

Satellite-to-satellite attitude control of a long-distance spacecraft formation for the Next Generation Gravity Mission

Original

Satellite-to-satellite attitude control of a long-distance spacecraft formation for the Next Generation Gravity Mission / Canuto, Enrico; Colangelo, Luigi; Lotufo, MAURICIO ALEJANDRO; Dionisio, S.. - In: EUROPEAN JOURNAL OF CONTROL. - ISSN 0947-3580. - STAMPA. - 25:settembre 2015(2015), pp. 1-16. [10.1016/j.ejcon.2015.03.003]

Availability:

This version is available at: 11583/2569336 since: 2016-05-12T15:07:18Z

Publisher:

Elsevier

Published

DOI:10.1016/j.ejcon.2015.03.003

Terms of use:

This article is made available under terms and conditions as specified in the corresponding bibliographic description in the repository

Publisher copyright

Elsevier postprint/Author's Accepted Manuscript

© 2015. This manuscript version is made available under the CC-BY-NC-ND 4.0 license
<http://creativecommons.org/licenses/by-nc-nd/4.0/>. The final authenticated version is available online at:
<http://dx.doi.org/10.1016/j.ejcon.2015.03.003>

(Article begins on next page)

Satellite-to-satellite attitude control of a long-distance spacecraft formation for the Next Generation Gravity Mission

Enrico Canuto (1), Luigi Colangelo (1), Mauricio Lotufo (1), Sabrina Dionisio (2)

(1) Politecnico di Torino, Dipartimento di Automatica e Informatica

Corso Duca degli Abruzzi 24, 10129 Torino, Italy

enrico.canuto@polito.it, luigi.colangelo@polito.it, mauricio.lotufo@polito.it

(2) Thales Alenia Space Italia

Strada Antica di Collegno 253, 10135 Torino, Italy

sabrina.dionisio@thalesaleniaspace.com

Contact author

Enrico Canuto

tel. +39 011 090 7026

fax +39 011 090 7099

ABSTRACT

The paper presents the design and some simulated results of the attitude control of a satellite formation under study by the European Space Agency for the Next Generation Gravity Mission. The formation consists of two spacecraft which fly more than 200 km apart at an altitude from the Earth's ground of between 300 and 400 km. The attitude control must keep the optical axes of the two spacecraft aligned with a microradian accuracy (pointing control). This is made possible by specific optical sensors accompanying the inter-satellite laser interferometer, which is the main payload of the mission. These sensors allow each spacecraft to actuate autonomous alignment after a suitable acquisition procedure. Pointing control is constrained by the angular drag-free control, which is imposed by mission science (Earth gravimetry at a low Earth orbit), and must zero the angular acceleration vector below $0.01 \text{ microradian/s}^2$ in the science frequency band. This is made possible by ultrafine accelerometers from the GOCE-class, whose measurements must be coordinated with attitude sensors to

achieve drag-free and pointing requirements. Embedded Model Control shows how coordination can be implemented around the embedded models of the spacecraft attitude and of the formation frame quaternion. Evidence and discussion about some critical requirements are also included together with extensive simulated results of two different formation types.

KEYWORDS: drag-free control, pointing control, attitude control, gravimetry, hybridization

1 Introduction

The Next Generation Gravity Mission (NGGM) under study by the European Space Agency, will take advantage of the previous gravimetry missions GOCE [1] and GRACE [2]. It will consist of a long-distance formation of two satellites as in GRACE ($d_{nom} \geq 200$ km), where each spacecraft (S/C) will be controlled to be drag-free as in GOCE [3], [4]. As a significant advancement, satellite-to-satellite distance fluctuations will be measured by laser interferometry with an accuracy improvement of at least three orders of magnitude with respect to GRACE (see Table 1, row 3). The formation will fly in a polar orbit at an altitude of between 330 and 420 km, depending on the formation type, either inline or pendulum. The satellites $k = 1, 2$ ($k = 1$ denotes the leader and $k = 2$ the follower) fly on the same orbit in the inline formation, whereas, in the pendulum formation; they fly on slightly separated and crossing orbits. The range of the orbit altitude requires drag cancellation and formation control. Drag-free control is ensured by the ultrafine accelerometers of the GOCE mission.

The paper focuses on the formation attitude control during the science phase, whose requirements are demanding because of several reasons. Intersatellite distance fluctuations must be measured along the satellite-to-satellite line (SSL) which is defined as the line joining the satellite centers-of-mass (CoM) C_1 and C_2 in Figure 1. In a low-Earth orbit, the SSL can be materialized - it becomes a measurable physical object - by differential global navigation system instruments (GNSI). For the same purpose, NGGM will also employ interferometry.

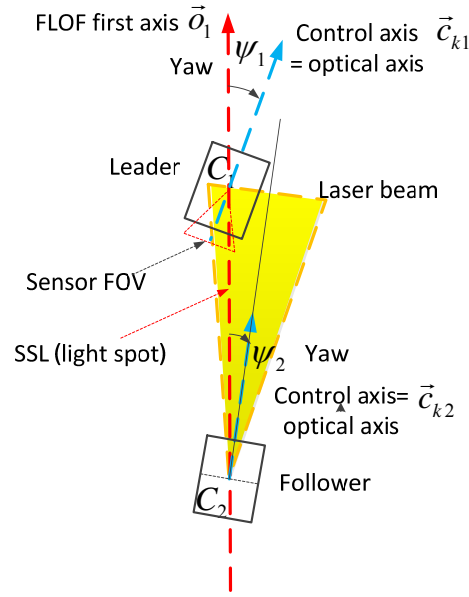


Figure 1 Sketch (not in scale) of the satellite-to-satellite line and of the laser beam.

One property of laser interferometry is that any direction inside a laser beam, which is launched by either satellite and is imaged by the receiving optics of the companion satellite, materializes the SSL (see Figure 1). The receiving optics fixes the first axis \vec{c}_{k1} of the k -th satellite, which must be perfectly aligned to the SSL by a 2D attitude control referred to as pointing control. Materialization errors occur because the SSL and the laser optical path do not coincide. An offset exists between CoM and optics, and the error magnitude can be shown to be of the order of the offset length ρ_k times the tilt q_k between \vec{c}_{k1} and the SSL. Error fluctuations limit the accuracy of the intersatellite distance measurement, which thus demands an upper bound to $|q_k|$. Assuming $|\rho_k| \leq 0.001$ m and nanometric distance accuracy, the spectral density of q_k must be of the order of $1 \mu\text{rad}/\sqrt{\text{Hz}}$ as in Table 1, row 7. This is the first challenging requirement of NGGM with respect to previous missions as reported in Table 1. Figure 2 shows the spectral bound (solid line) of the 2D pointing control, and the so-called science measurement bandwidth (MBW)

$$\mathfrak{N} = \{f_0 = 1 \text{ mHz} \leq f \leq f_1 = 100 \text{ mHz}\}, \quad (1)$$

where intersatellite distance measurement requires the highest accuracy. Here the term 'measurement' refers to science measurements during the mission, and not to attitude control measurements. Science data requirements demand formation attitude to be the most accurate in the MBW as shown by the 'minimum bound' in Figure 2 and by the 'drag-free bound' in Figure 3. Outside the MBW, science data accuracy progressively relax and consequently attitude requirements. The angular accuracy around \vec{c}_{k1} (the roll φ_k) is of the same order as in GRACE, but fluctuations must be rather slow in order to respect the angular-rate spectral bound of Table 1, row 9.

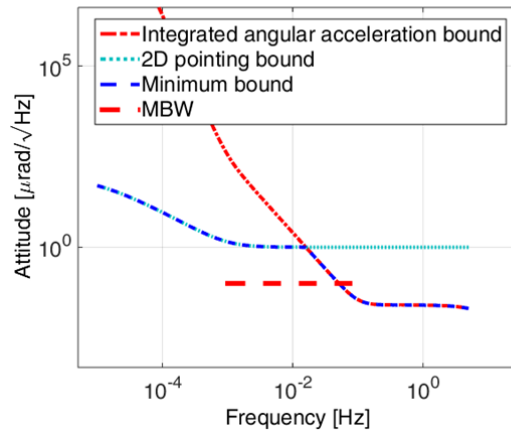


Figure 2 Spectral density bound of the 2D pointing control.

Table 1. Required bounds on attitude fluctuations of gravimetry missions				
No.	Requirements	GOCE	GRACE	NGGM
1	Orbit altitude [km]	250	500	330 (inline), 420 (pendulum)
2	Formation	None, single satellite	Two inline S/C 220 km apart	Two S/C 200 km apart
3	Intersatellite distance accuracy	None	10 μm [6]	0.005 $\mu\text{m}/\sqrt{\text{Hz}}$
4	3D angular acceleration max value [$\mu\text{rad}/\text{s}^2$]	1 [5]	1	1
5	3D angular acceleration spectral density [$\mu\text{rad}/\text{s}^2/\sqrt{\text{Hz}}$]	0.1 [5]	None	0.01
5	3D attitude max value [mrad]	150 [5]	4 [6]	See rows 6 to 9
6	2D pointing max value (pitch and yaw) [mrad]	See row 5	See row 5	0.02
7	2D pointing spectral density	None	None	0.001

	$\left[\text{mrad}/\sqrt{\text{Hz}} \right]$			
8	Roll max value [mrad]	See row 5	See row 5	2
9	3D angular rate spectral density $\left[\text{mrad/s}/\sqrt{\text{Hz}} \right]$	0.01 [5]	None	0.001
The term ‘spectral density’ stands for ‘root of unilateral Power Spectral Density’ (PSD). Spectral density bounds refer to the MBW				

SSL materialization and fine pointing can be obtained if the axis of the launched beam is more closely aligned with the SSL than the laser beam divergence, which is around 0.1 mrad. This alignment cannot be achieved by star trackers because of their bias which is of the same order or even larger. Optical sensors capable of measuring the beam tilt are mandatory [7]. If each satellite can image the incoming beam of the companion satellite, it becomes capable of autonomous alignment once the incoming laser spot has been located and held in the optics field-of-view. Optical tilt sensors are complemented with a pair of star trackers for implementing optical link acquisition and providing roll measurements. Gyroscopes are shown to be of scarce help.

A second set of requirements concerns the inertial angular acceleration (Table 1, rows 4 and 5) and the angular rate with respect to the local orbital frame of the mission, the so-called Formation Local Orbital Frame (FLOF), whose first axis \vec{o}_1 is directed along the SSL (see Figure 1). Their spectral density bounds in the MBW (Table 1, rows 4 and 9) are of the same order as in GOCE.

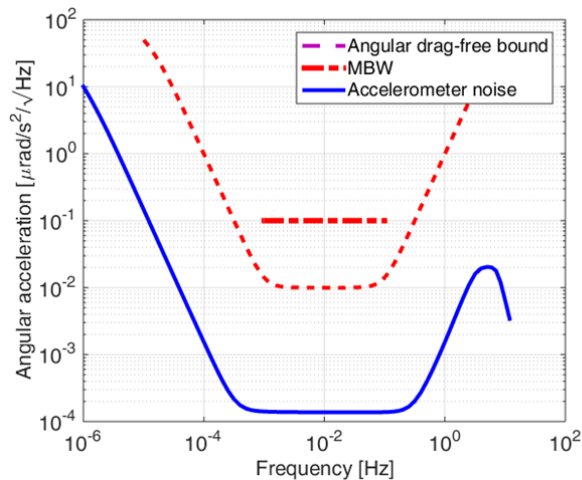


Figure 3 Drag-free bound and accelerometer noise.

The spectral bound (angular drag-free bound, dashed line) is shown in Figure 3 until the attitude control Nyquist frequency $f_{\max} = 0.5/T = 5$ Hz, where T is the control time unit. The bound has been designed to limit the errors of the accelerometer package which is employed by science to clean distance measurement from non-gravitational acceleration. The angular drag-free control is devoted to keeping angular acceleration below the required spectral bound. The same accelerometer package is employed for this purpose. The term ‘angular drag-free control’ is employed because it parallels the term ‘linear drag-free control’ [4]. Angular drag-free control is ideally required to zero the whole satellite angular acceleration, whereas linear drag-free control is required only to zero the non-gravitational accelerations, which justifies the term.

The second challenging requirement is to make the attitude control to satisfy at the same time acceleration, angular rate and attitude spectral requirements. In other words, the spectral density of the attitude command must also respect the angular drag-free bound of Figure 3. The same constraint has been plotted in Figure 2 from the attitude standpoint. If we denote the drag-free spectral bound in Figure 3 with $\bar{S}_a(f)$, the angular rate bound with $\bar{S}_\omega(f)$, and the pointing bound in Figure 2 with $\bar{S}_q(f)$, the minimal attitude bound $\bar{S}_{q,\min}(f)$ shown in Figure 2 (dashed line) is defined by

$$\bar{S}_{q,\min}(f) = \min \left\{ \bar{S}_q(f), \bar{S}_\omega(f)/\omega, \bar{S}_a(f)/\omega^2 \right\}. \quad (2)$$

Coordination between drag-free and pointing is referred to as ‘hybridization’, borrowing a term sometimes employed in the literature [8]. Hybridization usually refers to frequency coordination between inertial and position sensors with the purpose of enlarging position bandwidth (BW) and of guaranteeing sufficient accuracy despite poor accuracy and BW of position sensors. Here a control design solution is provided, as suggested by Figure 2, where the minimal attitude bound $\bar{S}_{q,\min}$ splits into two frequency bands. In the higher frequency band, say for $f > 10$ mHz, no attitude control effort need to be made since drag-free residuals already agree with pointing accuracy. In the lower frequency band, attitude control is

mandatory in order to cancel the drag-free residual drift and stabilize the attitude. Frequency decomposition naturally fits a hierarchical control scheme, where angular drag-free control is designed as a wide-band inner loop from DC up to the Nyquist frequency, and pointing control is designed as a narrow-band outer loop for guaranteeing attitude stability.

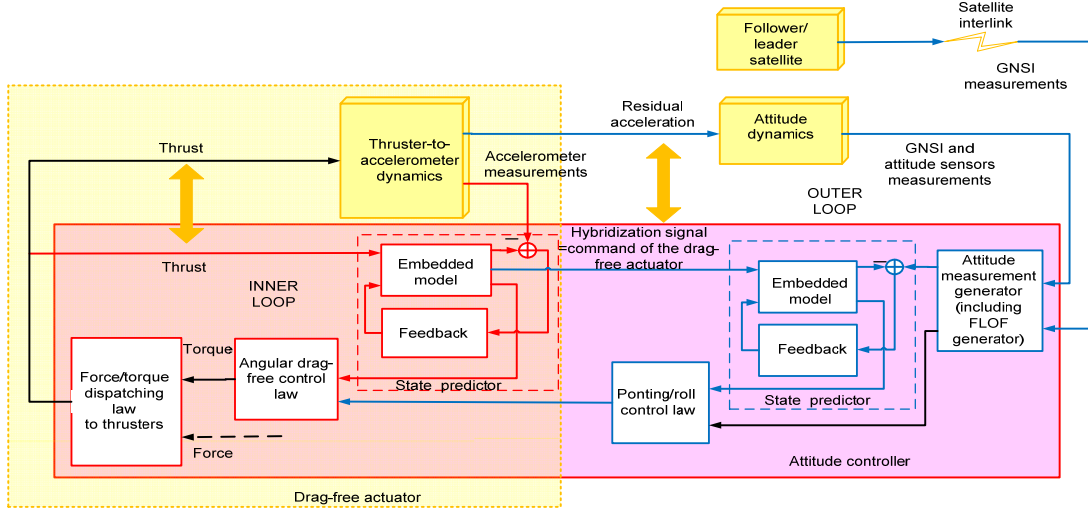


Figure 4 Block diagram of the hierarchical attitude controller.

The block diagram of the hierarchical attitude control system (ACS) is shown in Figure 4. The commanded torque and force vectors (the force is the output of the orbit and formation control [9]) merge in the dispatching law which provides the thrust vector to the satellite propulsion assembly. The attitude controller is the cascade, from right to left in Figure 4, of the pointing and roll controller (on the right side) and of the drag-free controller (on the left side). The latter builds up the overall attitude command by combining pointing and roll command with the drag-free one.

Hybridization requires that the 'hybridization signal' in Figure 4 is dispatched by the drag-free controller to the pointing embedded model. The signal looks like a feedback signal, but it is not. The signal simply bears out the Embedded Model Control principle [10], [11], [12], that the 'internal (or embedded) model' [13], [14], part of a control unit, must be driven by the same command which is dispatched to the plant. In fact, the signal is just the estimate of the residual acceleration which the drag-free controller actuates on each satellite. This concept is further

clarified by interpreting the whole drag-free controller in Figure 4 (state predictor and control law) as the attitude drag-free actuator. Double-sided arrows indicate the command signals entering both satellite and embedded models.

Coordinated attitude control of spacecraft formations is usually approached with the leader-follower strategy [15], [16], [17]. Each spacecraft follows another spacecraft in the formation, except the leader who tracks the absolute desired attitude trajectory of the formation. Another approach tries to decouple the individual attitude controller from the coordinated controller, in the sense that each spacecraft generates its own reference signals using the available information from other spacecraft [18]. This is similar to the present concept, since each spacecraft builds up the proper reference attitude from the differential GNSI measurements and from the incoming laser beam. In the present case of two spacecraft, the attitude reference turns out to be equal to the FLOF quaternion.

As shown by Figure 4, control functions are organized around two embedded models explained in Section 2. A third one is part of the FLOF generator. They include the controllable dynamics, namely thruster-to-accelerometer dynamics and spacecraft attitude dynamics, and a disturbance dynamics capable of describing the unknown disturbance class to be estimated and rejected. Disturbance dynamics generalizes the additional integrator of the extended state observers (ESO, [19]) in three ways. (i) State equations may have any order. (ii) The layout of the input noise vector must be designed in agreement with model uncertainty [3]. (iii) Each noise component is estimated by a dynamic filter- the noise estimator- driven by the model error, i.e. by measurement minus model output. The design of the dynamic filter will be referred as ‘noise synthesis’. The role of disturbance dynamics is essential for the drag-free and pointing control design. As such, the design methodology of this paper, to the authors’ knowledge, has no counterpart in the literature, except for the GOCE control design [3], [4]. The Design of spacecraft attitude control in the presence of disturbances has only recently received attention by the literature, but adopting standard ESO [20], [21]. One reason is that when high accuracy is demanded, spacecraft are placed at high-Earth-orbits where external disturbances become very low, and attitude dynamics is only perturbed by known gyro torques and appendage slow

vibrations [20]. A first-order ESO is usually sufficient to cope with their uncertainty. The spacecraft formation under study does not fall into this category.

The paper is organized as follows. Section 2 derives the three embedded models which are the core of the attitude controller. Each model is stabilized by a linear dynamic feedback, the ‘noise estimator’. Since quaternion dynamics, which is part of two models, is nonlinear, closed loop stability is proved with the help of a linear error equation. Section 3 explains and justifies hierarchical control design, and explains how the closed-loop eigenvalues of the three embedded models are optimized for achieving at the same time stability and performance. A special attention is devoted to ‘hybridization’ which drives the pointing controller design. Analytic design and simulated results point out some design criticalities. Recovery modes are also mentioned. This article is a revised and enlarged version of a conference paper [22].

2 Modeling

2.1 Frames of reference

Three main frames are necessary. (i) The Earth centered inertial frame $\mathcal{J} = \{C_E, \vec{i}_1, \vec{i}_2, \vec{i}_3\}$ has the origin in the Earth CoM C_E . (ii) The FLOF (Figure 5) $\mathcal{O} = \{C, \vec{o}_1, \vec{o}_2, \vec{o}_3\}$ is defined by the position vectors \vec{r}_1 and \vec{r}_2 of the leader and follower satellites, and has the origin in the formation CoM C . (iii) The control frame $\mathcal{C}_k = \{C_k, \vec{c}_{k1}, \vec{c}_{k2}, \vec{c}_{k3}\}$ of each satellite, $k = 1, 2$, has the origin in the CoM C_k . The control frame though different from the body frame, can be confused with the latter one in the present treatment. The FLOF is defined by

$$\vec{o}_1 = \frac{\vec{r}_1 - \vec{r}_2}{|\vec{r}_1 - \vec{r}_2|}, \quad \vec{o}_2 = \frac{\vec{r} \times \vec{o}_1}{|\vec{r} \times \vec{o}_1|}, \quad \vec{o}_3 = \vec{o}_1 \times \vec{o}_2 \quad (3)$$

where

$$d = |\Delta \vec{r}| = |\vec{r}_1 - \vec{r}_2|, \quad \vec{r} = \frac{\vec{r}_1 + \vec{r}_2}{2}, \quad |\vec{r}| = r. \quad (4)$$

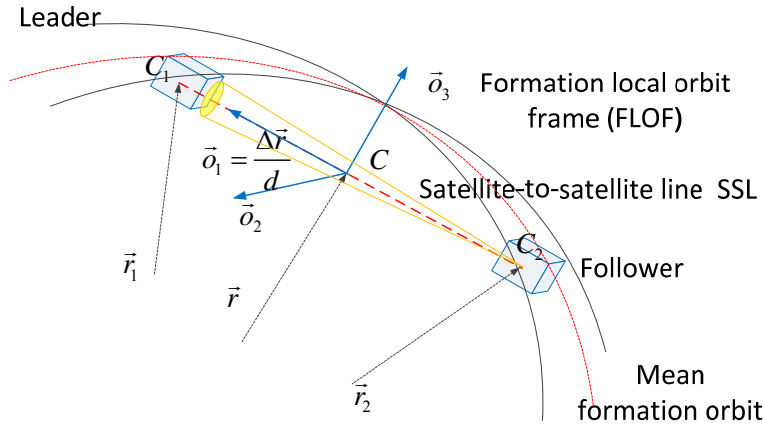


Figure 5 Formation local orbital frame for a pendulum formation.

Figure 5 shows the FLOF of a pendulum formation where polar orbits are separated by offsetting the right ascension of the ascending node. The SSL direction is \vec{o}_1 . The FLOF to inertial transformation is denoted by R_o^i and the relevant quaternion by \mathbf{q}_o ; it will be referred to as the 'FLOF quaternion'. The axis \vec{c}_{k1} is the axis to be aligned with \vec{o}_1 . The control to FLOF transformation is denoted by $R_{ck}^o = Z(\psi_k)Y(\theta_k)X(\phi_k)$ and the quaternion \mathbf{q}_k is referred to as the 'local control quaternion'. Pointing control is concerned with ψ_k (yaw) and θ_k (pitch). The 'local quaternion' in the inertial frame holds $\mathbf{q}_{ck} = \mathbf{q}_o \otimes \mathbf{q}_k$, where the symbol \otimes denotes quaternion multiplication. Since subscript k will be hereafter dropped, previous quaternion equation is rewritten as

$$\mathbf{q}_c = \mathbf{q}_o \otimes \mathbf{q}. \quad (5)$$

Scalar and vector components of a quaternion are defined as follows

$$\mathbf{q} = q_0 \begin{bmatrix} 1 \\ \mathbf{q}/2 \end{bmatrix}, \quad \mathbf{q} = \begin{bmatrix} q_1 \\ q_2 \\ q_3 \end{bmatrix} \cong \begin{bmatrix} \phi \\ \theta \\ \psi \end{bmatrix}. \quad (6)$$

The rightmost approximation in (6) holds when Euler angles are very small, i.e. $|\phi|, |\theta|, |\psi| \ll 1 \text{ rad}$, which is the present case.

2.2 Embedded and design models

Embedded Model Control distinguishes between the design and embedded model. The design model provides definition and realization of the class of the ‘true’ performance variables, say the local quaternion \mathbf{q} in (5). The embedded model is the core of the control unit: state variables are marked by a hat like $\hat{\mathbf{q}}$ and are available as control signals. Other variables such as noise and errors are marked with a bar like $\bar{\mathbf{w}}$. Errors between embedded model variables and ‘true’ variables, say $\hat{\mathbf{e}}_q = \mathbf{q}^{-1} \otimes \hat{\mathbf{q}}$, are the key performance variables. In the Kalman filter framework errors like $\hat{\mathbf{e}}$ are referred to as prediction/estimation errors, here as ‘design errors’. The embedded model, in the discrete-time (DT) form, is enriched with uncertainty/disturbance dynamics, whose state variables are the repository of the past uncertainty. Disturbance dynamics may be assumed to be stochastic dynamics and is driven by a DT white noise to be real-time estimated. Angular accelerations are denoted either with the symbol \mathbf{a} when radian/s^2 is the unit, or with $\boldsymbol{\alpha}$ when the radian is the unit. The embedded model minimal time unit is the same as the attitude control and is denoted by $T = 0.1 \text{ s}$. DT instants are denoted by $t_i = iT$ or simply by i . Measured variables are marked by a round hat as $\tilde{\mathbf{q}}$.

The model is subdivided into three parts: (i) the FLOF quaternion dynamics (subscript o) predict reference quaternion, angular rate and acceleration, (ii) the attitude dynamics (subscript q) predict spacecraft attitude and disturbance, (iii) the thruster to accelerometer dynamics (or drag-free dynamics) (subscript a) predict the environment acceleration to be cancelled. The section ends with the derivation of the error equation of $\hat{\mathbf{e}}_q$, which lays the ground for the noise estimator design.

2.3 FLOF dynamics

The FLOF design model is just the quaternion kinematics

$$\begin{aligned} \dot{\mathbf{q}}_o(t) &= \mathbf{q}_o(t) \otimes \boldsymbol{\omega}_o(t) / 2, \quad \mathbf{q}_o(0) = \mathbf{q}_{o0} \\ \tilde{\mathbf{q}}_o(j) &= \mathbf{q}_o(j) \otimes \mathbf{e}_o(j) \end{aligned} \quad (7)$$

where $\tilde{\mathbf{q}}_o$ is the measurement which is computed from differential GNSI data using the FLOF definition (3) and the mean orbit angular rate ω_{nom} :

$$|\dot{\boldsymbol{\omega}}_o| \cong \omega_{nom} \cong 1.18 \text{ mrad/s}, f_{nom} = (2\pi)^{-1} \omega_{nom} \cong 0.2 \text{ mHz}, \quad (8)$$

GNSI measurements are sampled at $t_j = jNT$, $N \geq 1$. The angular rate $\dot{\boldsymbol{\omega}}_o$ and the acceleration $\ddot{\boldsymbol{\omega}}_o$, to be employed as reference signals by attitude control, are unknown and must be estimated. The embedded model consists of the DT version of (7) and of third-order stochastic dynamics, which latter accounts for the class of the unknown signals. The model is written as follows

$$\begin{aligned} \hat{\boldsymbol{q}}_o(j+1) &= c_o \hat{\boldsymbol{q}}_o(j) + s_o \hat{\boldsymbol{q}}_o(j) \otimes \hat{\mathbf{v}}_o(j)/2, \quad \hat{\boldsymbol{q}}_o(0) = \hat{\boldsymbol{q}}_{o0}, \\ \hat{\mathbf{x}}_o(j+1) &= A_o \hat{\mathbf{x}}_o(j) + \bar{\mathbf{w}}_o(j), \quad \hat{\mathbf{x}}_o(0) = \hat{\mathbf{x}}_{o0}, \end{aligned} \quad (9)$$

where,

$$\begin{aligned} c_o &= \cos(\hat{\omega}_o NT/2), s_o = \sin(\hat{\omega}_o NT/2)/(\hat{\omega}_o NT/2) \\ \hat{\omega}_o &= |\dot{\boldsymbol{\omega}}_o|, \quad \hat{\mathbf{v}}_o(j) = \dot{\boldsymbol{\omega}}_o(j) NT, \quad |\hat{\boldsymbol{q}}_o(j)| = 1 \\ A_o &= \begin{bmatrix} I & I & 0 \\ 0 & I & I \\ 0 & 0 & I \end{bmatrix}, \quad \hat{\mathbf{x}}_o = \begin{bmatrix} \hat{\mathbf{v}}_o \\ \hat{\boldsymbol{\alpha}}_o \\ \hat{\mathbf{s}}_o \end{bmatrix}, \quad \bar{\mathbf{w}}_o = \begin{bmatrix} \bar{\mathbf{w}}_{o1} \\ \bar{\mathbf{w}}_{o2} \\ \bar{\mathbf{w}}_{o3} \end{bmatrix}, \quad I = I_3 \end{aligned} \quad (10)$$

All the state variables are in radian units: $\hat{\mathbf{v}}_o$ is a DT angular rate, $\hat{\boldsymbol{\alpha}}_o$ is the low-frequency component of $\dot{\boldsymbol{\omega}}_o$ and $\hat{\mathbf{s}}_o$ is a DT jerk. $\bar{\mathbf{w}}_o$ is an unknown zero-mean arbitrary vector (noise for short) driving the stochastic dynamics in (9). When $N > 1$, (9) should be propagated during any step j to match the attitude control times iT . In reality, since the attitude control BW is close to $0.002f_{\max} = 0.01 \text{ Hz}$ and $N \leq 10$, propagation becomes not strictly necessary, and for simplicity's sake we assume $N=1$ and $j=i$. The third-order model of the angular rate is justified by the FLOF acceleration $\ddot{\boldsymbol{\omega}}_o$ not being zero, but dominated by the orbit first harmonic as in

$$\dot{\boldsymbol{\omega}}_o(t) = \mathbf{a}_{o1} \sin(\omega_{nom}t + \phi_1) + \dots, \quad |\mathbf{a}_{o1}| \leq 10^{-3} \mu\text{rad/s}^2, \quad (11)$$

where ω_{nom} has been defined in (8). Step-wise interpolation of (11) would correspond to second-order dynamics in (10) and to an error of about $|\Delta\dot{\boldsymbol{\omega}}_o| \approx \omega_{nom} |\mathbf{a}_{o1}| T < 2 \times 10^{-6} \mu\text{rad/s}^2$. As a consequence, the attitude error would turn out to be close to $2 \mu\text{rad}$, of the same order of the pointing accuracy in Table 1. Adopting third-order dynamics as in (10) eliminates the issue.

2.4 Attitude dynamics

The design model of the local attitude \mathbf{q} in (5) is the following

$$\begin{aligned}\dot{\mathbf{q}}(t) &= \mathbf{q}(t) \otimes \boldsymbol{\omega}(t) / 2, \quad \mathbf{q}(0) = \mathbf{q}_0 \\ \dot{\boldsymbol{\omega}}(t) &= J^{-1}(\mathbf{M}_u(t) + \mathbf{M}_d(t)) - d(R_o^c \boldsymbol{\omega}_o) / dt, \quad \boldsymbol{\omega}(0) = \boldsymbol{\omega}_0, \\ \mathbf{a}(t) &= J^{-1}(\mathbf{M}_u(t) + \mathbf{M}_d(t)) = \mathbf{a}_u(t) + \mathbf{d}(t)\end{aligned}\quad (12)$$

where \mathbf{a} is the spacecraft acceleration to be ideally zeroed in the MBW. The rightmost term in the second equation approximates the FLOF acceleration defined in (11):

$$d(R_o^c \boldsymbol{\omega}_o) / dt = R_o^c \dot{\boldsymbol{\omega}}_o - \boldsymbol{\omega} \times R_o^c \boldsymbol{\omega}_o \cong \dot{\boldsymbol{\omega}}_o. \quad (13)$$

In (12), \mathbf{M}_u is the commanded torque in control coordinates, \mathbf{M}_d is the total disturbance torque in control coordinates, and includes gyro, gravity gradient and aerodynamic torques, J is the inertia matrix. Commanded torques are actuated by a thruster assembly. Gyro and gravity gradient torques, though depending on angular rate and attitude, are not explicitly reported, since they are treated as unknown components of \mathbf{M}_d , ready to be cancelled by drag free control.

The embedded model is the same as in (9), except that the noise vector $\bar{\mathbf{w}}_q$ is accompanied by the residual acceleration $\bar{\mathbf{a}}$ - the hybridization signal - which is generated by the drag-free embedded model, and by the FLOF acceleration $\hat{\mathbf{a}}_o$ in (10). The model is written as

$$\begin{aligned}\hat{\mathbf{q}}(i+1) &= c(i) \hat{\mathbf{q}}(i) + s(i) \hat{\mathbf{q}}(i) \otimes \hat{\mathbf{v}}_q(i) / 2, \quad \hat{\mathbf{q}}(0) = \hat{\mathbf{q}}_0 \\ \hat{\mathbf{x}}_q(i+1) &= A_q \hat{\mathbf{x}}_q(i) + B_q (\bar{\mathbf{a}}(i) - \hat{\mathbf{a}}_o(i)) + \bar{\mathbf{w}}_q(i), \quad \hat{\mathbf{x}}_q(0) = \hat{\mathbf{x}}_{q0}, \\ \check{\mathbf{q}}(i) &= \hat{\mathbf{q}}_o^{-1}(i) \otimes \check{\mathbf{q}}_c(i) = \hat{\mathbf{q}}(i) \otimes \bar{\mathbf{e}}_q(i)\end{aligned}\quad (14)$$

where c and s have similar expressions as c_o and s_o in (10), the vectors $\hat{\mathbf{x}}_q$ and $\bar{\mathbf{w}}_q$ have similar components as the vectors in (10) upon subscript change, and the matrices hold $A_q = A_o$ and $B_q^T = [I \quad 0 \quad 0]$. In agreement with (5), the local attitude measurement $\check{\mathbf{q}}$ is obtained from the FLOF quaternion prediction $\hat{\mathbf{q}}_o$ in (9) and from the control quaternion measurement $\check{\mathbf{q}}_c$ in (14). $\check{\mathbf{q}}_c$ is computed by combining star tracker and optical metrology data. $\bar{\mathbf{e}}_q$ is the model error.

To better understand how the second equation in (12) matches its counterpart in (14), the equation of the angular rate $\hat{\mathbf{v}}_q = \hat{\boldsymbol{\omega}}T$ - in radian units - is made explicit:

$$\begin{aligned} \hat{\mathbf{v}}_q(i+1) - \hat{\mathbf{v}}_q(i) &= \bar{\mathbf{a}}(i) + \hat{\mathbf{a}}_q(i) + \bar{\mathbf{w}}_{q1}(i) - \hat{\mathbf{a}}_o(i) \\ \mathbf{a}(i)T^2 &\cong \bar{\mathbf{a}}(i) + \hat{\mathbf{a}}_q(i) + \bar{\mathbf{w}}_{q1}(i) \end{aligned} \quad (15)$$

In (15), the estimated residual $\bar{\mathbf{a}}$ is corrected by the unknown disturbance $\hat{\mathbf{a}}_q + \bar{\mathbf{w}}_{q1}$, which accounts for accelerometer errors, and includes bias, drift and noise. In other terms, accelerometer errors are modelled in (15) as an unknown disturbance to be rejected by the attitude control [23]. More specifically, only the prediction $\hat{\mathbf{a}}_q$ will be explicitly rejected. Rejection aims to keep the drift of the integrated residuals in Figure 2 - the dotted line diverging toward the left side - below the pointing bound in the same Figure. The noise term $\bar{\mathbf{w}}_{q1}$ cannot be predicted and is not rejected. The model (14) is affected by a neglected dynamics $\partial\mathbf{P}_q$, which includes thruster dynamics and attitude sensor delay. The known part of the delay may be included in (14), but to be conservative, $\partial\mathbf{P}_q$ is assumed to include the whole delay.

2.5 Drag-free model

The acceleration measurement $\tilde{\mathbf{a}}$, sampled at iT , is related to \mathbf{a} in (12) by a linear dynamics \mathbf{P}_a which accounts for the dynamic chain from thruster to accelerometer, and includes second-order thruster dynamics (see Table 3). Using Z-transform we write

$$\begin{aligned} \tilde{\mathbf{a}}(z) &= \mathbf{P}_a(z)\mathbf{a}(z) + \mathbf{d}_a(z) \\ \bar{\mathbf{d}}_a(i)T^2 &= -(\hat{\mathbf{a}}_q(i) + \bar{\mathbf{w}}_{q1}(i)) \end{aligned} \quad (16)$$

where \mathbf{d}_a denotes the accelerometer errors and is estimated by the unknown disturbance $\hat{\mathbf{a}}_q$ in (15). GOCE drag-free control design [4] has shown, and experimental performance has confirmed that \mathbf{P}_a in (16) can be approximated by a delay of length T . The transfer function of the neglected dynamics can be written as $\partial\mathbf{P}_a(z) = \mathbf{M}_a^{-1}(z)\mathbf{P}_a(z) - I_3$, where $\mathbf{M}_a(z) = z^{-1}I_3$ accounts for the model delay. The embedded model writes as

$$\begin{aligned} \hat{\mathbf{x}}_a(i+1) &= A_a\hat{\mathbf{x}}_a(i) + B_a\mathbf{a}_u(i) + \bar{\mathbf{w}}_a(i), \quad \hat{\mathbf{x}}_a(0) = \hat{\mathbf{x}}_{a0} \\ \tilde{\mathbf{a}}(i) &= C_a\hat{\mathbf{x}}_a(i) + \bar{\mathbf{e}}_a(i) \end{aligned} \quad (17)$$

where $\bar{\mathbf{e}}_a$ is the model error and \mathbf{a}_u is the whole attitude and drag-free command. The noise vector $\bar{\mathbf{w}}_a$ has the same components as $\bar{\mathbf{w}}_o$ in (10) and $\bar{\mathbf{w}}_q$ in (14) upon subscript change. Matrices and vectors have the following components

$$A_a = \begin{bmatrix} 0 & I & 0 \\ 0 & I & I \\ 0 & 0 & I \end{bmatrix}, B_a = B_q, \mathbf{x}_a = \begin{bmatrix} \hat{\mathbf{z}}_a \\ \hat{\mathbf{a}}_a \\ \hat{\mathbf{s}}_a \end{bmatrix}, C_a = \begin{bmatrix} 1 & 0 & 0 \end{bmatrix}. \quad (18)$$

All the variables in (18) are angular accelerations [rad/s²] and $\hat{\mathbf{z}}_a$ is the delayed measurement.

2.6 Design error equations

2.6.1 Error definition

Models (9), (14) and (17) point out the synthesis problems to be done at each step i :

- 1) to estimate the vectors $\bar{\mathbf{w}}_o(i)$, $\bar{\mathbf{w}}_q(i)$ and $\bar{\mathbf{w}}_a(i)$ for updating disturbance/uncertainty dynamics;
- 2) to predict the command $\mathbf{a}_u(i+1)$ which will be actuated during the next time step,
- 3) to estimate the residual acceleration $\bar{\mathbf{a}}(i)$ - in radian units - entering (14).

The following errors are the performance variables of the control design.

- 1) The design error (usually prediction/estimation error) is defined by $\hat{\mathbf{e}}_v = \mathbf{v} - \hat{\mathbf{v}}$, where \mathbf{v} and $\hat{\mathbf{v}}$ are the state vectors of the design and embedded models: it is the performance variable of the noise (estimator) synthesis.
- 2) The true tracking error is defined by $\mathbf{e}_v = \underline{\mathbf{v}} - \mathbf{v}$, where $\underline{\mathbf{v}}$ is the reference variable: it is the performance variable of the command synthesis.

The above errors converge to each other if $\hat{\mathbf{v}}(i) + \underline{\mathbf{v}}(i) \rightarrow 0$, in which case control design restricts to the noise synthesis. Assuming the above convergence sounds reasonable, since $\hat{\mathbf{v}}$ and $\underline{\mathbf{v}}$ are just model variables generated by the embedded models. In reality, because the estimated noise vectors $\bar{\mathbf{w}}(i)$ cannot be predicted and rejected, the zero limit cannot be reached, but it remains a desirable target and may be referred to as the ‘anti-causal limit’ as in [11], [12]. Therefore, noise synthesis turns out to be the main tool for guaranteeing performance and stability. In fact, drag-free command only actuates disturbance rejection and only depends

on the noise synthesis (Section 3.3). Pointing and roll command include also reference and state feedback, but state feedback, despite being essential for attitude stability, is just tuned not to worsen noise synthesis performance (Section 3.4). In the next two sub-sections, analysis of the design error equations proves that noise synthesis becomes linear and time invariant (LTI) also in the case of quaternion equations, and that tunable parameters are the disturbance dynamics order and the state predictor BW (Proposition 1). The second parameter is obvious, but the former goes beyond ESO literature.

2.6.2 Design error equations

We derive the error equation of the attitude model (14). Similar equations apply to the FLOF model (9) and to the drag-free model (17). In the Appendix, Section 6.1, the DT equation of the vectorial part $\hat{\mathbf{e}}_q$ of the design error $\hat{\mathbf{e}}_q = \hat{\mathbf{q}}^{-1} \otimes \mathbf{q}$ - see (6) - is shown to satisfy

$$\hat{\mathbf{e}}_q(i+1) = (I - \hat{\boldsymbol{\omega}}(i)T \times) \hat{\mathbf{e}}_q(i) + (\boldsymbol{\omega}(i) - \hat{\boldsymbol{\omega}}(i))T, \quad \hat{\mathbf{e}}_q(0) = \hat{\mathbf{e}}_{q0}. \quad (19)$$

Equation (19) must be related to the measurement $\tilde{\mathbf{q}}$ in (14) and to the ‘true’ model error $\mathbf{e}_q = \mathbf{q}^{-1} \otimes \tilde{\mathbf{q}}$ which is not measurable. The measured error $\bar{\mathbf{e}}_q$, defined in (14), which is available in the control unit, is related to $\hat{\mathbf{e}}_q$ through the equality

$$\bar{\mathbf{e}}_q(i) = \hat{\mathbf{q}}^{-1}(i) \otimes \tilde{\mathbf{q}}(i) = \hat{\mathbf{q}}^{-1}(i) \otimes \mathbf{q}(i) \otimes \mathbf{e}_q(i) = \hat{\mathbf{e}}_q(i) \otimes \mathbf{e}_q(i). \quad (20)$$

Equation (19) must be completed with the error equation of $\hat{\mathbf{x}}_q$, which has the same form as (14), namely

$$\tilde{\mathbf{x}}_q(i+1) = A_q \tilde{\mathbf{x}}_q(i) + B_q \mathbf{w}_q(i) - \bar{\mathbf{w}}_q(i), \quad \tilde{\mathbf{x}}_q(0) = \tilde{\mathbf{x}}_{q0}. \quad (21)$$

In (21), $\tilde{\mathbf{x}}_q$ is a 3×3 vector as $\hat{\mathbf{x}}_q$ and has 3-dimensional components $\tilde{\mathbf{x}}_{qh}$, $h=1,2,3$. The first component $\tilde{\mathbf{x}}_{q1} = (\boldsymbol{\omega} - \hat{\boldsymbol{\omega}})T$ is the input vector of (19). Discrepancies between (12) and (14) are confined into \mathbf{w}_q through the equality

$$\begin{aligned} \mathbf{w}_q(i) = & \left(T \int_{iT}^{(i+1)T} \left(J^{-1} \mathbf{M}_d(\tau) - \hat{\mathbf{a}}_a(i) \right) d\tau - \hat{\mathbf{a}}_q(i) \right) - \\ & - \left(T \left(R_c^o \boldsymbol{\omega}_o(i+1) - R_c^o \boldsymbol{\omega}_o(i) \right) - \hat{\mathbf{a}}_o(i) \right) \end{aligned} \quad (22)$$

which is obtained, after some substitution, from (12), (14) and the control laws which are derived in Section 3. The left bracket in (22) contains drag-free residuals, but they are cleaned from the accelerometer drift $\hat{\mathbf{a}}_q$ which is predicted by the attitude model (14). The right bracket is the design error of the FLOF acceleration $\dot{\mathbf{w}}_o$ in (11), and combines GNSI measurement errors and errors due to higher-order gravity harmonics. A nonlinear term $|\hat{\mathbf{w}}(i)T \times \hat{\mathbf{e}}_q(i)|$ of the order of $|\mathbf{e}_q(t)|^2$ can be eliminated from (19), which turns out to be LTI and decoupled like (21). This assumption holds due to the following inequalities from Table 1:

$$\begin{aligned} |\hat{\omega}_1 T| &\leq 5 \mu\text{rad} < |e_{q1}| \leq 2 \text{ mrad (roll)} \\ |\hat{\omega}_j T| &\leq 5 \mu\text{rad} < |e_{qj}| \leq 20 \mu\text{rad}, j = 2, 3 \text{ (pitch and yaw)} \end{aligned} \quad (23)$$

As a result, error equations (19), (20) and (21) convert into a series of four 3-dimensional and decoupled integrators, driven by $\bar{\mathbf{w}}_q$ and \mathbf{w}_q , which is written in compact form as

$$\begin{aligned} \tilde{\mathbf{x}}_e(i+1) &= A_e \tilde{\mathbf{x}}_e(i) + B_e \mathbf{w}_q(i) - G_e \bar{\mathbf{w}}_q(i), \quad \tilde{\mathbf{x}}_e(0) = \tilde{\mathbf{x}}_{e0}, \\ \bar{\mathbf{e}}_q(i) &= C_e \tilde{\mathbf{x}}_e(i) + \mathbf{e}_q(i) \end{aligned} \quad (24)$$

and has the following matrices and vectors

$$\begin{aligned} A_e &= \begin{bmatrix} I_3 & 0 \\ 0 & A_q \end{bmatrix}, \quad G_e = \begin{bmatrix} 0 \\ I_9 \end{bmatrix}, \quad B_e = \begin{bmatrix} 0 \\ B_q \end{bmatrix}, \quad \tilde{\mathbf{x}}_e = \begin{bmatrix} \hat{\mathbf{e}}_q \\ \tilde{\mathbf{x}}_q \end{bmatrix}, \\ C_e &= [I \quad 0], \dim \bar{\mathbf{w}}_q = 9 < \dim \tilde{\mathbf{x}}_e = 12 \end{aligned} \quad (25)$$

Equation (24) is observable by $\bar{\mathbf{e}}_q$ and controllable by $\bar{\mathbf{w}}_q$.

2.6.3 Stability of the error equations

Assuming that \mathbf{w}_q and \mathbf{e}_q are independent of $\tilde{\mathbf{x}}_e$, (24) can be stabilized by the output-to-state feedback

$$\bar{\mathbf{w}}_q(z) = \mathbf{L}_q(z) \bar{\mathbf{e}}_q(z), \quad (26)$$

where Z-transform has been adopted since the feedback gain $\mathbf{L}_q(z)$ is in general a transfer matrix. The feedback (26) will be referred to as ‘noise estimator’, and applies to each of the embedded models upon replacement of the subscript q with o and a . The input-output closed-loop transfer matrix holds

$$\begin{aligned}
\tilde{\mathbf{x}}_e(z) &= \mathbf{S}_e(z) \mathbf{M}_e(z) \mathbf{w}_q(z) - \mathbf{V}_e(z) \bar{\mathbf{e}}_q(z) \\
\mathbf{M}_e &= (zI - A_e)^{-1} B_e, \quad \mathbf{S}_e(\Lambda_q) = \left(I + (zI - A_e)^{-1} G_e \mathbf{L}_q(z) C_e \right)^{-1} \\
\mathbf{V}_e(\Lambda_q) &= \mathbf{S}_e(zI - A_e)^{-1} G_e \mathbf{L}_q(z)
\end{aligned} \tag{27}$$

In (27), \mathbf{S}_e is the sensitivity matrix and Λ_q is the spectrum of the closed-loop dynamic system which consists of (24) and (26). Λ_q is referred to as the ‘state-predictor spectrum’, though the state predictor, which consists of (12) and (26), is nonlinear. Stability of \mathbf{S}_e is not sufficient if \mathbf{w}_q and \mathbf{e}_q depend on $\tilde{\mathbf{x}}_e$. To simplify stability conditions, we assume that only \mathbf{w}_q is state-dependent as follows

$$\mathbf{w}_q(i) = \mathbf{w}_{q0}(\tilde{\mathbf{y}}_q, i) + W_q(\tilde{\mathbf{y}}_q, i) \tilde{\mathbf{x}}_e(i), \quad |W_q| < 1, \tag{28}$$

where $\tilde{\mathbf{y}}_q$ is the prediction error of an exogenous variable \mathbf{y}_q , like the total disturbance torque \mathbf{M}_d in (12), which is predicted by (14). The small gain theorem [28] guarantees closed-loop stability if

$$\max_{|f| < f_{\max}} \left| \mathbf{S}_e(jf, \Lambda_q) \mathbf{M}_e(jf) \right| |W_q| < 1. \tag{29}$$

Here the main purpose is to prove that under (28), $|W_q|$ tends to decrease as soon as the prediction ahead time h decreases and the order n of the disturbance dynamics increases. The result offers the designer tunable parameters for guaranteeing stability and performance.

Proposition 1. Consider (28) and assume that the exogenous vector $\mathbf{y}_q(t)$, $\dim \mathbf{y}_q = m$, is a bounded signal with bounded derivatives $\mathbf{y}_q^{(n)}$. Assume that the matrix $W_q(\tilde{\mathbf{y}}_q(t), t)$ is a sector-bounded function of the prediction error $\tilde{\mathbf{y}}_q = \mathbf{y}_q - \hat{\mathbf{y}}_q$, i.e.

$$-W_{qj} \leq \frac{W_q(\tilde{\mathbf{y}}_q(t), t)}{\tilde{y}_{qj}(t)} \leq W_{qj}, \quad 0 \leq W_{qj}, j = 1, \dots, m, \tag{30}$$

where y_{qj} is a component of $\mathbf{y}_q(t)$. Let n be the order of the disturbance dynamics in charge of predicting $\mathbf{y}_q(t+h)$, $h > 0$. Then

$$\left| W_q(\tilde{\mathbf{y}}(t), t) \right| \leq \gamma(m, n) \max_{j=1, \dots, m} W_{qj} \max_{0 \leq \mathcal{G} < h} \left| \mathbf{y}_q^{(2)}(t + \mathcal{G}) \right| h^n, \tag{31}$$

where $\gamma(m, n) < \infty$ is a constant, $|\mathbf{y}_q| = \max_j |y_{qj}|$, $|W_q|$ is the matrix of the absolute values of W_q and $\max_{j=1, \dots, m} W_{qj}$ is obtained componentwise.

Proof. Assume $n = 2$ for simplicity's sake. The prediction at $t + h$ can be 'exactly' written as the sum of the prediction $\hat{\mathbf{y}}_q(t + h)$, available at time t , and of the prediction error $\tilde{\mathbf{y}}_q(t + h)$. Let us start from the exact expansion of $\mathbf{y}_q(t + h)$:

$$\begin{aligned} \mathbf{y}_q(t + h) &= \mathbf{y}_q(t + \theta_0) + \mathbf{y}_q^{(1)}(t + \theta_1)h + \mathbf{y}_q^{(2)}(t + \theta_2)h^2 / 2 \\ 0 \leq \theta_k < h, \quad k &= 0, 1, 2 \end{aligned} \quad (32)$$

Further expansion around t of the zero- and first-order terms in (32) yields the final expression:

$$\begin{aligned} \mathbf{y}_q(t + h) &= \hat{\mathbf{y}}_q(t + h) + \tilde{\mathbf{y}}_q(t + h) \\ \hat{\mathbf{y}}_q(t + h) &= \mathbf{y}_q(t) + \mathbf{y}_q^{(1)}(t)(1 + \theta_0 / h)h \\ \tilde{\mathbf{y}}_q(t + h) &= \mathbf{y}_q^{(2)}(t + \vartheta_0)\theta_0^2 / 2 + \mathbf{y}_q^{(2)}(t + \vartheta_1)\theta_1 h + \mathbf{y}_q^{(2)}(t + \theta_2)h^2 / 2 \\ 0 \leq \vartheta_j < h, \quad j &= 0, 1, \quad 0 \leq \theta_k < h, \quad k = 0, 1, 2 \end{aligned} \quad (33)$$

The prediction $\hat{\mathbf{y}}_q(t + h)$ is the free response of a second-order integrator. The prediction error, which depends on the unknown $\mathbf{y}_q^{(2)}(t + \vartheta)$, is bounded by

$$|\tilde{\mathbf{y}}_q(t + h)| \leq \max_{0 \leq \vartheta < h} 5 |\mathbf{y}_q^{(2)}(t + \vartheta)| h^2 / 2. \quad (34)$$

Using (30) and (34), and the norm definitions in the Proposition statement, one finds the inequality

$$\begin{aligned} |W_q(\tilde{\mathbf{y}}(t), t)| &\leq \gamma(m, 2) \max_{j=1, \dots, m} W_{qj} \max_{0 \leq \vartheta < h} |\mathbf{y}_q^{(2)}(t + \vartheta)| h^2, \\ \gamma(m, 2) &= 5m / 2 \end{aligned} \quad (35)$$

which can be extended to arbitrary n as in (31). \square

Remark 1. The ahead time h corresponds to the predictor time constant, which is fixed by Λ_q . Decreasing h forces the predictor bandwidth to increase, in agreement with high-gain observer theorems [29]. Moreover, since the predictor BW is bounded in order to attenuate the neglected dynamics effect, the low-frequency slope of the sensitivity \mathbf{S}_e in (29) which is proportional to n [11], [12], offers a further degree of freedom.

3 Hierarchical control design

3.1 Control requirements and rationale

Drag-free and pointing/roll controllers are strictly designed around the embedded models (9), (14) and (17). Three basic principles, coordinate decoupling, hierarchy and frequency coordination guide the design.

- 1) Decoupling allows the 3D error equation in (24) to split into three separate single-input-single-output models.
- 2) Hierarchy allows to write \mathbf{a}_u in (17) as the sum of the drag-free command \mathbf{a}_{DF} and of the pointing/roll command $\boldsymbol{\alpha}_{PR}$ (in radian units):

$$\begin{aligned}\mathbf{a}_u(i) &= \mathbf{a}_{DF}(i) + \boldsymbol{\alpha}_{PR}(i) / T^2 \\ \mathbf{a}_{DF}(i) &= -\hat{\mathbf{a}}_a(i, \Lambda_a) \\ \boldsymbol{\alpha}_{PR}(i) &= \hat{\boldsymbol{\alpha}}_o(i, \Lambda_o) - \hat{\boldsymbol{\alpha}}_q(i, \Lambda_q) - (K_q(\Lambda_c) \hat{\mathbf{q}}(i) + K_v(\Lambda_c) \hat{\mathbf{v}}(i))\end{aligned}\quad (36)$$

In (36), Λ_a is the spectrum of the drag-free predictor which consists of (17) and of a feedback term like (26). Λ_o is the spectrum of the FLOF generator which consists of the equation (9) and the output feedback (26). Λ_q enters (27) and Λ_c is the spectrum of the controllable dynamics in (14), when it is closed by the state feedback of the third equation in (36).

In (36) \mathbf{a}_{DF} is ideally designed to zero the acceleration \mathbf{a} in the MBW, which objective is obtained by cancelling the predicted acceleration $\hat{\mathbf{a}}_a$ of (18). $\boldsymbol{\alpha}_{PR}$ is ideally designed to zero local control attitude, angular rate and acceleration in (12), i.e. to achieve

$$\begin{aligned}\mathbf{q}(iT) &= q_0(iT) \begin{bmatrix} 1 \\ \mathbf{q}(iT)/2 \end{bmatrix} = \underline{\mathbf{q}}(i) = \begin{bmatrix} 1 \\ 0 \end{bmatrix} \\ \boldsymbol{\omega}(iT) = 0 &\Rightarrow \boldsymbol{\omega}_c(iT) \cong \boldsymbol{\omega}_o(iT) \\ \dot{\boldsymbol{\omega}}(iT) = 0 &\Rightarrow \mathbf{a}(iT) \cong \dot{\boldsymbol{\omega}}_o(iT)\end{aligned}\quad (37)$$

The symbol \cong indicates that the control to FLOF transformation has been neglected, i.e. $R_o^c \cong I_3$. In order to achieve (37), $\boldsymbol{\alpha}_{PR}$ must track the FLOF acceleration $\hat{\mathbf{a}}_o$, cancel the drift $\hat{\boldsymbol{\alpha}}_q$ and include a state feedback for stabilizing attitude and angular rate.

- 3) Hybridization, namely frequency coordination between inner and outer loop, makes the overall spectral requirements to be met.

Actual requirements are expressed in terms of spectral densities, and only concern random components. Deterministic components, mainly due to orbit harmonics, must be bounded by the RMS of each spectral line, a requirement not reported in Table 1. Acceleration and attitude requirements are given in terms of the spectral matrices \mathbf{S}_a^2 and \mathbf{S}_q^2 by the following inequalities

$$\begin{aligned} I_3 \bar{\mathbf{S}}_a^2(f) - \mathbf{S}_a^2(f) &\geq 0 \\ \bar{\mathbf{S}}_q^2(f) - \mathbf{S}_q^2(f) &\geq 0, \quad \bar{\mathbf{S}}_q^2 = \text{diag}\{\bar{\mathbf{S}}_{q1}^2, \bar{\mathbf{S}}_{q,\min}^2, \bar{\mathbf{S}}_{q,\min}^2\} \end{aligned} \quad (38)$$

where $\bar{\mathbf{S}}_{q1}$ refers to roll and $\bar{\mathbf{S}}_{q,\min}$, defined in (2), refers to pointing control. Similar inequalities apply to $\boldsymbol{\omega}$ in (37). The bounds $\bar{\mathbf{S}}_a$ and $\bar{\mathbf{S}}_{q,\min}$ are plotted in Figure 2 and Figure 3, respectively.

3.2 Coordinate decoupling

Coordinate decoupling splits the estimate of the 3D noise vectors in (9), (14) and (17) into three single-input noise estimators, and the feedback transfer matrix $\mathbf{L}_q(z)$ in (26) becomes diagonal. Decoupling is not mandatory. For instance, by adopting Kalman filter approach, the whole feedback gain $\mathbf{L}_q(z) = \mathbf{L}_q$ would become static and determined by the joint covariance of input and output noise. Three reasons prevent this approach.

- 1) The noise covariance of \mathbf{w}_q is not available. This difficulty may be bypassed by designing an equivalent spectral density, where ‘equivalent’ means that is shaped in a manner to envelope the disturbing torque class. This is exactly the way that will be employed here for tuning closed-loop eigenvalues.
- 2) The driving noise \mathbf{w}_q and the model error $\mathbf{e}_q(i)$ in (24) depend on the model state in an uncertain way, which requires robust eigenvalue tuning.
- 3) The noise estimator (26) may be required to be a dynamic feedback, in which case, as shown in the Appendix, the state predictor is not equivalent to a Kalman filter.

Robust eigenvalue tuning is greatly simplified by coordinate decoupling. Decoupling is also suggested by the error equation (24) as it is LTI and decoupled. A decoupled tuning must guarantee stability and performance versus state dependent uncertainty. Small gain theorem will be employed to the purpose, and design error will be replaced by tracking error.

3.3 Hierarchy: drag-free control design

Hierarchical control aims at tuning the four spectra \mathcal{A}_h , $h = a, o, q, c$ entering (36) in order to guarantee the target inequalities (38). Tuning is tackled in a hierarchical way.

- 1) Estimation of $\hat{\mathbf{a}}_a$ (drag), $\hat{\mathbf{a}}_q$ (accelerometer bias and drift) and $\hat{\mathbf{a}}_o$ (FLOF) in (36) is decoupled. Drag is estimated from accelerometer measurements, bias and drift from attitude sensor measurements (a pair of star trackers and optical metrology), FLOF acceleration from GNSI measurements. Decoupling is coherent with Figure 6, which compares the angular drag-free bound with the doubly integrated noise of the attitude sensors. Also the doubly integrated noise affecting $\hat{\mathbf{a}}_o$ in (36) and due to differential GNSI is shown (dashed line).
- 2) Tuning of the four spectra is done in sequence, by firstly requiring that the drag-free spectrum \mathcal{A}_a guarantees the former inequality in (38). The last three spectra are then tuned to satisfy both inequalities in (38) as outlined in Section 3.4.

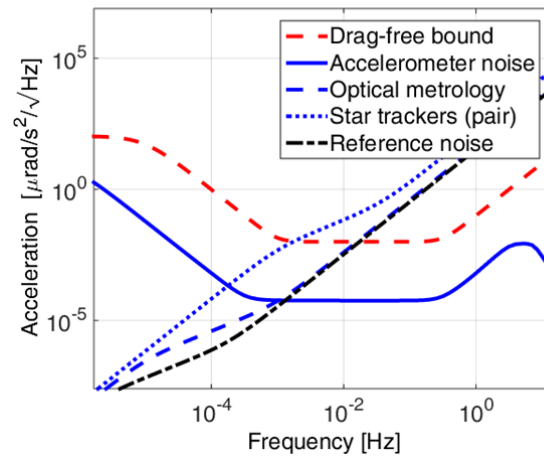


Figure 6 Angular accelerometer error compared with attitude sensor noise.

Let us \mathcal{D} and \mathcal{D}_a denote the classes of the disturbance \mathbf{d} in (12) (drag) and of \mathbf{d}_a in (16) (accelerometer error) which are estimated by $\hat{\mathbf{a}}_a$ and $\hat{\mathbf{a}}_q$. The class \mathcal{D} is defined by expanding the generic component d_k , $k=1,2,3$, as follows

$$d_k(t) = \sum_{n=0}^{\infty} d_{kn} \sin(n2\pi f_{nom} + \phi_{nk}) + d_{kr}(t), \quad (39)$$

where f_{nom} is defined in (8). In (39) d_{kr} is a wide-band colored noise accounting for thruster noise. The line spectrum d_{kn} accounts for the drag periodic components that decay in proportion to n^{-2} . In the frequency band $f \geq f_{d0} = 0.01$ Hz, the PSD $\mathbf{S}_d^2(f)$ of \mathbf{d} is dominated by d_{kr} and is bounded by

$$\begin{aligned} \mathbf{S}_d^2(f) &\leq I_3 \bar{S}_d(f) = I_3 \left(S_{d0}^2(f_{d0}/f)^2 + S_{d1}^2 \right) \\ S_{d0} &= 5 \times 10^{-6} \text{ rad/s}^2/\sqrt{\text{Hz}}, f_{d0} = 0.03 \text{ Hz}, S_{d1} = 1 \times 10^{-9} \text{ rad/s}^2/\sqrt{\text{Hz}}. \end{aligned} \quad (40)$$

Figure 6 points out that star trackers may improve the estimation accuracy of \mathbf{d} for $f < f_{nom}$ and optical sensors for $f < f_{d0}$. A similar inequality to (40), $\mathbf{S}_{da}^2(f) \leq I_3 \bar{S}_{da}^2(f)$, defines the class \mathcal{D}_a . Proposition 2, below, gives sufficient conditions for the residual acceleration \mathbf{a} to satisfy (38). In this case, the noise estimator (26) simplifies into the static feedback

$$\bar{\mathbf{w}}_a(i) = L_a \bar{\mathbf{e}}_a(i) \quad (41)$$

since the size $n_w = 3 \times 3$ of the noise vector in (17) is the same as the state vector (see the Appendix, Section 6.2). The drag-free controller sensitivity \mathbf{S}_a is defined as the DT transfer matrix from the ‘true’ disturbance $\mathbf{d}(iT)$ to the residual acceleration $\mathbf{a}(iT)$ in (12), after having zeroed other exogenous signals, namely

$$\begin{aligned} \mathbf{a}(z) &= \mathbf{S}_a(z) \mathbf{d}(z) \\ \mathbf{V}_a(z) &= I - \mathbf{S}_a(z). \end{aligned} \quad (42)$$

Sensitivity and complementary sensitivity \mathbf{V}_a are diagonal matrices due to decoupling.

Proposition 2. Under the disturbance classes \mathcal{D} and \mathcal{D}_a , a sufficient condition for \mathbf{a}_{DF} in (36) to guarantee the first inequality in (38), is that any component of \mathbf{a} satisfies the spectral inequality

$$W_a(f, \eta_a, A_a) = \eta_a W_{sa}(f, A_a) + (1 - \eta_a) W_{va}(f, A_a) \leq 2\eta_a < 2, f \leq f_{\max}, \quad (43)$$

where

$$\begin{aligned} W_{sa}(f) &= \frac{1}{\bar{S}_a(f)} \sqrt{|\mathbf{S}_a(f)|^2 \bar{S}_d^2(f) + |\mathbf{V}_a(f)|^2 \bar{S}_{da}^2(f) + \bar{S}_{PR}^2(f)}, \\ W_{va}(f) &= |\mathbf{V}_a(jf)| \partial \bar{P}_a(jf) \end{aligned} \quad (44)$$

and \bar{S}_{PR} is the spectral bound of the pointing/roll command in (36).

Proof. As a sketch of proof, let us rewrite the Z-transform of $\mathbf{a}(iT)$ in (12) as follows

$$\mathbf{a}(z) = \mathbf{a}_u(z) + \mathbf{d}(z) = \mathbf{a}_{PR}(z)/T^2 - \hat{\mathbf{a}}_a(z) + \mathbf{d}(z). \quad (45)$$

Then compute $\hat{\mathbf{a}}_a$ from (17) and (41), with the help of (42), which yields

$$\begin{aligned} \hat{\mathbf{a}}_a(z) &= \mathbf{V}_a(z)(\mathbf{d}(z) + \mathbf{d}_a(z) + z\mathbf{e}_a(z)) \\ z\mathbf{e}_a(z) &= \partial \mathbf{P}_a(z) \mathbf{a}(z) \end{aligned} \quad (46)$$

where the neglected dynamics $\partial \mathbf{P}_a$ is bounded by $|\partial \mathbf{P}_a(jf)| \leq \partial \bar{P}_a(jf)$ and \mathbf{e}_a is the ‘true’ model error as opposed to the measured error $\bar{\mathbf{e}}_a$. Replacing (46) in (45) provides

$$\mathbf{a}(z) = (I + \mathbf{V}_a(z) \partial \mathbf{P}_a(z))^{-1} (\mathbf{a}_{PR}(z)/T^2 + \mathbf{S}_a(z) \mathbf{d}(z) - \mathbf{V}_a(z) \mathbf{d}_a(z)). \quad (47)$$

Using small gain theorem, a sufficient stability condition is

$$|\mathbf{V}_a(jf)| \partial \bar{P}_a(jf) \leq \eta_a < 1. \quad (48)$$

The inequality (43) derives from (48) and by rewriting the first spectral inequality in (38) with the help of (47). \square

The LHS term in (43) can be minimized with respect to Λ_a in order to guarantee a design margin. Optimization has been performed by fixing $\eta_a = 0.5$, by assuming $S_{PR} = 0$, and by simplifying the complementary spectrum $\Gamma_a = 1 - \Lambda_a$ into a single unknown parameter as $\Gamma_a = \{\gamma_a, \gamma_a, 2\gamma_a\}$.

The functional $\max_{0 \leq f \leq f_{\max}} W_a(\eta_a = 0.5, \gamma_a)$ and the components in (43) are plotted in Figure 7 versus $\gamma_a = 2\pi f_a T$. The optimal solution falls in the range $0.2 \leq \gamma_a \leq 0.3$ and corresponds to the frequency band $0.3 \leq f_a \leq 0.5$ Hz. The drag-free control looks feasible in the large since the functional (43) is less than unit in the decade $0.07 \leq \gamma_a \leq 0.6$. Figure 7 shows the magnitude diagram of $|\mathbf{S}_a|$ and of $|\mathbf{V}_a|$ in (42). In the same Figure, W_{as} decreases for f_a

increasing, which fact is in agreement with drag cancellation. The opposite behavior of W_{av} , which depends on the neglected dynamics through $|\mathbf{V}_a| \partial \bar{P}_a$, places an upper limit to the drag-free BW f_a .

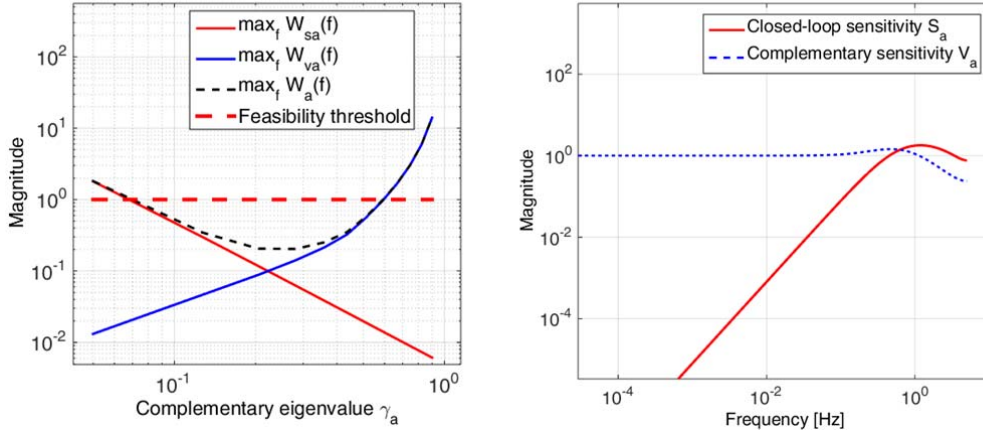


Figure 7 Left: design functional. Right: sensitivity and complementary sensitivity.

One may wonder why the noise estimator (41) has not been optimized as a steady-state Kalman feedback. The reason is that the model error \mathbf{e}_a in (46) is noise free, since the accelerometer noise \mathbf{d}_a , from DC to the Nyquist frequency, has been treated as an input disturbance. At the same time \mathbf{e}_a is affected by neglected dynamics, and the latter substitutes the measurement noise in (43).

3.4 Hybridization: pointing control

Because of the sub-milliradian bounds in Table 1, the ‘true’ attitude components become the entries of \mathbf{q} in (6). Each of the pointing components q_2 and q_3 must satisfy the spectral bound in Figure 2. The roll q_1 is only required by Table 1, row 8, to be bounded in time, and to have smooth fluctuations as required by the angular rate bound in Table 1, row 9. A roll spectral bound can be adjusted as in Figure 8, by combining the integrated bound of the angular rate with the temporal bound. Figure 2 is repeated in Figure 8 by adding the spectral density of the star tracker noise and of the optical metrology noise.

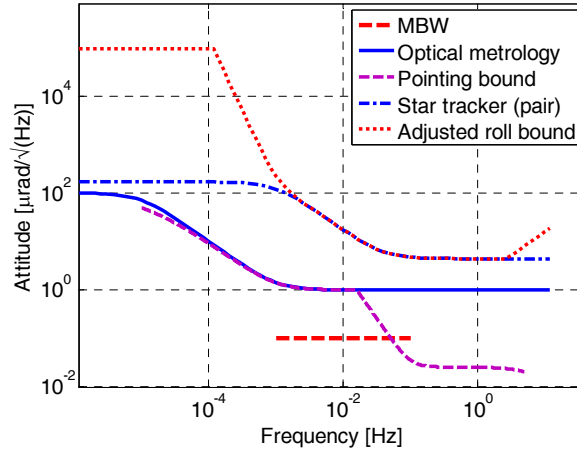


Figure 8 Pointing and roll bound compared to attitude sensor noise.

Figure 2 and Figure 8 suggest decomposing pointing and roll control objectives as follows:

- 1) to cancel the accelerometer drift and bias in the frequency band $f < 1$ mHz (the leftmost drift in Figure 2),
- 2) to filter the optical metrology noise for $f > 10$ mHz in order to respect the pointing limit imposed by the drag-free bound in Figure 2,
- 3) to bound the satellite attitude versus the neglected dynamics $\partial \mathbf{P}_q$.

The combination of the former two objectives is referred to as ‘hybridization’. They are each other contrasting, implying that the problem may be unfeasible. In fact, it will be shown that, given present requirements and noise spectral densities, the pointing bound in Figure 2 can only be approached from above especially in the frequency band $1 \text{ mHz} < f < 10 \text{ mHz}$.

Unlike drag-free control design in Section 3.3, the third objective is dominated by the second one as in the Kalman filter approach, since the control BW of the frequency coordination becomes much smaller than the BW which guarantees the attitude to be bounded versus $\partial \mathbf{P}_q$. Kalman optimization cannot be pursued since a noise estimator which is capable of providing $\bar{\mathbf{w}}_q$ in (14) cannot be static as in (41), but it must be dynamic as proved in the Appendix, Section 6.2. In fact, the size $n_w = 3 \times 3$ of $\bar{\mathbf{w}}_q$ is less than the size $n = 4 + 3 \times 3 - 1 = 12$ of the state vector (the quaternion constraint has been accounted for). Moreover, it is shown in the

Appendix, Section 6.3, that the resulting state equation belongs to a class of state predictors which is different from stationary Kalman filters.

One may wonder why a static estimator is not employed, despite the different size of noise and state vectors. Indeed, it could be employed, but a parasitic noise should be inserted in the quaternion equation (14) to the detriment of the closed-loop complementary sensitivity $\mathbf{V}_q = \mathbf{I} - \mathbf{S}_q$. In fact, under a static feedback, the high-frequency asymptote of \mathbf{V}_q only decays of -20 dB/decade, but, under a dynamic feedback, it decays of -40 dB /decade, without any price to be paid by \mathbf{S}_q . A larger decay helps approaching the second control objective - sensor noise filtering - without penalizing sensitivity.

Because of the unitary difference $\Delta n = (n - n_w) / 3 = 1$, a first-order dynamic feedback is sufficient, namely

$$\begin{aligned} \mathbf{p}_q(i+1) &= (1 - \delta_q) \mathbf{p}_q(i) + \bar{\mathbf{e}}_q(i) \\ \bar{\mathbf{w}}_q(i) &= N_q \mathbf{p}_q(i) + L_q \bar{\mathbf{e}}_q(i) \end{aligned} \quad (49)$$

The gain matrices L_q and M_q in (49) together with the feedback gains K_q and K_v in (36), are tuned so as to satisfy the three previous objectives.

Before dealing with gain tuning, we must prove that the estimate $\bar{\mathbf{a}}$ of the residual acceleration in (14) – the ‘hybridization signal’- drives the attitude predictor in the same manner as the drag-free controller actuates the spacecraft. We require that

$$\bar{\mathbf{a}}(i) = \mathbf{a}_{PR}(i) + \bar{\mathbf{a}}_{DF}(i), \quad (50)$$

where \mathbf{a}_{PR} is the pointing/roll command and $\bar{\mathbf{a}}_{DF}(i)$ is the estimate of the wide-band drag-free residuals, in radian units, driving the attitude. With the help of (17) and (18), the current estimate $\bar{\mathbf{a}}$ of the residual acceleration \mathbf{a} holds

$$\bar{\mathbf{a}}(i) = \bar{\mathbf{a}}_a(i) + \bar{\mathbf{w}}_{a1}(i) + \mathbf{a}_u(i) = T^2 \mathbf{a}_{PR}(i) + \bar{\mathbf{a}}_a(i) - \hat{\mathbf{a}}_a(i) + \bar{\mathbf{w}}_{a1}(i), \quad (51)$$

where $\bar{\mathbf{a}}_a$ is the second entry of the drag-free state estimate $\bar{\mathbf{x}}_a(i) = \hat{\mathbf{x}}_a(i) + K_a \bar{\mathbf{e}}_a(i)$ and

$$L_a = \begin{bmatrix} L_{a0} \\ L_{a1} \\ L_{a2} \end{bmatrix} = A_a K_a = \begin{bmatrix} K_{a1} \\ K_{a1} + K_{a2} \\ K_{a2} \end{bmatrix} \quad (52)$$

defines the estimate gain K_a on the basis of the feedback gain L_a in (41). Since the matrix A_a in (18) turns out to be singular, (52) has a unique solution if and only if $A_a - L_a C_a$ preserves three zero eigenvalues, in other words if $L_{a1} = L_{a0} + L_{a2}$. From (51) and (52) one finds that

$$\bar{\mathbf{a}}_{DF}(i) = (K_{a1} + L_{a1}) \bar{\mathbf{e}}_a(i) T^2, \quad (53)$$

The hybridization signal $\bar{\mathbf{a}}_{DF}$ is therefore a wide-band bounded signal, since it is proportional to the innovation $\bar{\mathbf{e}}_a$, i.e. to the output of the stabilized error equation (24).

The set of spectra $\Lambda = \{\Lambda_q, \Lambda_c, \Lambda_o\}$ is tuned in a similar manner as the drag-free design. If (50) holds, the following equality, which is the analogue of (47), can be proved

$$\begin{aligned} \mathbf{q}(z) = & -\mathbf{S}_q(z, \Lambda_q, \Lambda_c) (\mathbf{M}_q(z) \mathbf{d}_a(z) + \tilde{\mathbf{q}}_o(z)) - \mathbf{V}_q(z, \Lambda_q, \Lambda_c) \mathbf{e}_q(z) \\ \mathbf{M}_q = & (z-1)^{-2} T^2, \mathbf{V}_q = I - \mathbf{S}_q \end{aligned} \quad (54)$$

where \mathbf{e}_q has been defined in (24) and \mathbf{d}_a is the accelerometer bias/drift in (16). The design error $\tilde{\mathbf{q}}_o$ of the FLOF generator has an expression similar to (54).

Equation (54) and the second inequality in (38) can be converted into

$$W_q(f, \eta_q, \Lambda) = \eta_q W_{sq}(f, \Lambda) + (1 - \eta_q) W_{vq}(f, \Lambda) \leq 2\eta_q < 2, f \leq f_{\max}, \quad (55)$$

which is similar to (43) and has the following components

$$\begin{aligned} W_{sq}(f) = & \frac{1}{\bar{S}_q(f)} \sqrt{|\mathbf{S}_q(f)|^2 \left(|\mathbf{M}_q|^2 \bar{S}_{da}^2(f) + \bar{S}_{qo}^2(f) \right) + |\mathbf{V}_q(f)|^2 \bar{S}_{qs}^2(f)} \\ W_{vq}(f) = & |\mathbf{V}_q(jf)| \left| \partial \bar{P}_q(jf) \right|, \left| \partial \mathbf{P}_q(jf) \right| \leq \partial \bar{P}_q(jf) \end{aligned} \quad (56)$$

In (56) \bar{S}_{da} defines the class \mathcal{D}_a of the accelerometer drift, \bar{S}_{qo} is the spectral bound of the FLOF generator error and \bar{S}_{qs} is the bound of the attitude sensor noise. The components are assumed to be uncorrelated. Assuming $W_{vq}(f) \ll 1$, we can force $\eta_q = 1$, thus eliminating the contribution of $\partial \mathbf{P}_q$ and simplifying (55) to the first term.

Minimization of $\max_{0 \leq f \leq f_{\max}} W_q(f, \eta_q = 1, \Lambda)$ is more complex than (43), due to the large size of eigenvalues which is equal to $n_q = 5 + 5 + 2$ for each axis. Coordinate decoupling has been exploited, by minimizing (55) for each axis. The n_q degrees of freedom have been reduced to

five by correlating the elements of the spectrum $\Lambda(j)$, $j = x, y, z$, of the generic axis, in the following manner

$$\begin{aligned}\lambda_{oh}(j) &\in \Lambda_o(j) = 1 - \gamma_{q0}(j) \delta(j) 2^{-h\beta(j)}, \quad \delta(j) > 1, \quad \gamma(j) \geq 0, \quad h = 0, 1, \dots, 4 \\ \lambda_{qh}(j) &\in \Lambda_q(j) = 1 - \gamma_{q0}(j) 2^{-h\alpha(j)}, \quad 0 < \gamma_{q0}(j) \leq 1, \quad \alpha(j) \geq 0, \quad h = 0, 1, \dots, 4 . \\ \lambda_{ch}(j) &\in \Lambda_c(j) = 1 - \gamma_{q0}(j) \kappa(j), \quad \kappa(j) \gg 1, \quad h = 0, 1\end{aligned}\quad (57)$$

The rules of the first and second rows aim to spread the spectrum below $f_{q0} = (2\pi T)^{-1} \gamma_{q0}$ (attitude state predictor) and $f_o = (2\pi T)^{-1} \gamma_{q0} \delta$ (FLOF generator) in order to reduce the sensitivity and complementary sensitivity overshoot [26], [27]. Overshoot limitation aims not to amplify residual disturbance components (those not cancelled), and in turn the state feedback magnitude. α and β are referred to as ‘spreading exponents’. The FLOF generator upper frequency $f_o(j)$ turns out to be wider than the attitude predictor and requires $\delta(j) > 1$. The third rule tends to approach (without reaching) the anti-causal condition of the Embedded Model Control [10], [11], [12], which suggests that the state feedback spectrum $\Lambda_c(j)$ is closer to zero (deadbeat control) than the state predictor $\Lambda_q(j)$. This aim requires $\kappa(j) \gg 1$. Design parameters in (57) were firstly obtained from a simplified optimization of (55). Results were then adjusted by a pre-defined sequence of simulated runs. Table 2 summarizes optimization results.

Table 2. Drag-free and pointing/roll eigenvalues					
No.	Control function	Complementary eigenvalue bound	Frequency upper bound [Hz]	Spreading exponent	Size
1	3D FLOF generator	0.1	0.16	1.5	6
2	2D pointing state predictor (pitch, yaw)	0.005	0.008	1.2	6
3	Roll state predictor	0.002	0.003	2	6
4	3D state feedback	0.1	0.16	0	2
5	3D angular drag-free	0.5	0.8	1.7	3
6	Time unit [s]	0.1			

Figure 9, left, shows the functional $\max_{0 \leq f \leq f_{\max}} W_q(f, \eta_q = 1, \Lambda) / 2$ versus the upper bound $\gamma_{q0}(j = 2, 3)$ of the complementary eigenvalues in (57) for pointing control axes. The three plotted curves point out that pointing control design does not respect (55), since the functional stays always above the unit upper bound. The case with $\kappa = 1$ proves that increasing κ , in

other words, widening the state feedback BW (toward the anti-causal limit) is of benefit. The case $\alpha = 1.5$ aims to further reduce the overshoot of the sensitivity in Figure 9, right, but at the same time narrows the overall control BW without any benefit to the functional value. The case $\kappa(j) = 20$ and $\alpha(j) = 1.2$, $j = 2, 3$, which appears to be insensitive to γ_{q0} from 0.002 to about 0.01, was taken as the best solution. The optimal value $\gamma_{q0} = 0.005$ was found experimentally within the insensitive range.

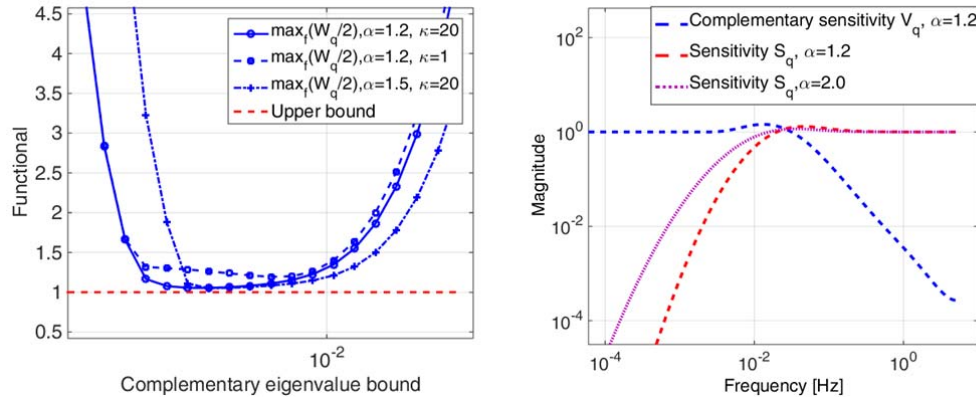


Figure 9 .Left: design functional. Right: sensitivity and complementary sensitivity.

The fact that the design does not conform to (55), implies that also the second inequality (38) is not respected, as shown by simulated results in Section 4. Two are the main reasons.

- 1) The BW of the FLOF generator must be sufficiently wide in order to estimate the FLOF acceleration. The reference noise density in Figure 6, due to GNSI measurements, combined with optical metrology noise, makes the overall sensor noise to increase.
- 2) Filtering the optical metrology noise by narrowing the state predictor BW, for instance by increasing the spreading exponent α in (57), is constrained by the need of rejecting the residual acceleration drift.

As a conclusion, the spectral pointing bound in Table 1, row 7, should be considered a worst-case objective. Alternative, relaxed spectral bounds have been issued by science as shown in Section 4.

Finally, fiber optical gyroscopes seem of scarce help for pointing control. Assume a noise spectral density of $\tilde{S}_\omega \cong 1 \mu\text{rad}/(\text{s}\sqrt{\text{Hz}})$, which is typical of navigation grade gyroscopes. Integration along the MBW (from 1 mHz to 100 mHz) provides the angular spectral density $\tilde{S}_q \cong 1.6 \div 160 \mu\text{rad}/\sqrt{\text{Hz}} \geq \bar{S}_{q,\min}$ which is larger than the pointing bound in (38) and in Table 1, row 7.

4 Simulated results

Simulated results were obtained from the end-to-end mission simulator which was jointly developed by Thales Alenia Space Italia and Politecnico di Torino. Two different orbits were simulated, inline and pendulum. Orbital, mass and environment parameters are in Table 3. Thruster assembly parameters are provisional, since layout is still to be frozen.

Table 3. Orbit, mass and environment parameters					
No.	Parameter	Unit	Value		Comment
			Inline formation	Pendulum formation	
1	Semimajor axis	km	$R_E + 335$	$R_E + 419$	$R_E \cong 6378\text{km}$
2	Eccentricity		0.001	0.001	
3	Inclination	rad	1.553 (89 deg)	1.553 (89 deg)	
4	Right ascension of the ascending node	rad	1.571 (90 deg)	$1.5721 \pm \pm 0.0013(\Delta\Omega)$	RAAN
5	Perigee anomaly	rad	$\pm 0.0149(\Delta\omega)$	$\pm 0.0149(\Delta\omega)$	
5	True anomaly	rad	0	0	Initial
6	Pendulum aperture	rad	0	$\pm 0.0872(5 \text{ deg})$	$\cong \Delta\Omega / \Delta\omega$
6	Solar radio flux	$\frac{10^{-22} \text{ W}}{\text{m}^2 \text{ Hz}}$	$73 \div 240$	$73 \div 240$	Variable
7	Geomagnetic index	nT	18	18	
8	Mass	kg	885	885	
9	Inertia matrix	kgm^2	$\begin{bmatrix} 230 & -14 & 6 \\ -14 & 1700 & 1 \\ 6 & 1 & 1600 \end{bmatrix}$	$\begin{bmatrix} 230 & -14 & 6 \\ -14 & 1700 & 1 \\ 6 & 1 & 1600 \end{bmatrix}$	
10	Thrust range	mN	$0.05 \div 2.5$	$0.05 \div 2.5$	Provisional
11	Thruster angular frequency	rad/s	25	25	2 nd order response

Attitude control assumes a diagonal inertia matrix J_{nom} affected by a few percent of uncertainty. Thruster and accelerometer dynamics is simplified to be a 0.1 s delay. The noise spectral density of the optical metrology is in Figure 8. The results are obtained from short-run simulations lasting 2×10^5 s (about 2 and half days). Spectral densities are plotted in the frequency band $0.01 \text{ mHz} \leq f \leq 100 \text{ mHz}$, which overlaps the MBW. Figures refer to the leader satellite; the follower having similar profiles. Angular components are denoted with x (roll), y (pitch) and z (yaw).

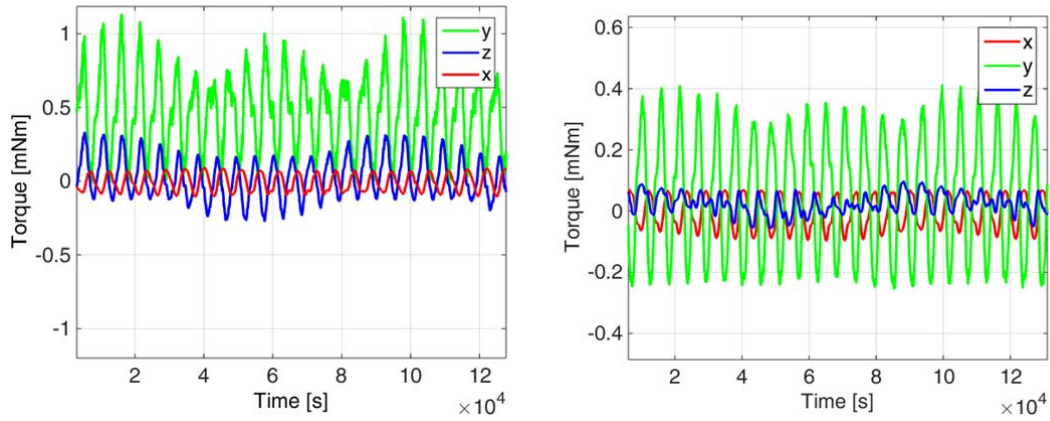


Figure 10 Perturbation torques. Left: inline formation. Right: pendulum formation.

Figure 10 shows the total environment torque \mathbf{M}_d in (12), free of thruster noise and gyro torque. Pendulum formation torques, Figure 10, appear to be smaller than inline formation torques because of higher altitude. Magnitude modulation is due to the daily variable solar activity which modifies the thermosphere density (the residual density at low-Earth-orbits, which is highly sensible to solar activity). Assuming one-meter thruster arm, 1 mNm torque corresponds to 1 mN thrust, in agreement with Figure 11, where the commanded thrust vector is plotted. The plotted command includes translational drag-free and formation command [9]. The thrust vector magnitude of the pendulum formation is smaller than the thrust bound of 2.5 mN in Table 3, but it is closer to the bound for the inline formation. A low margin of this kind is mainly due to translational drag-free controller and not to attitude controller. The low margin,

although of primary concern, can be enlarged by optimizing the thruster assembly layout, a design task be done in parallel with thruster technology finalization and assessment. The margin may be slightly increased by partly actuating commanded torques with magnetic torquers, since they are mandatory as backup actuators. The issue of how to manage possible thrust saturation is not treated here, but it is strictly related with the long-term solar activity prediction. In fact, the magnitude of aerodynamic forces and torques is proportional to the thermosphere density, and the NGGM mission life is planned to last about ten years, close to the solar activity period.

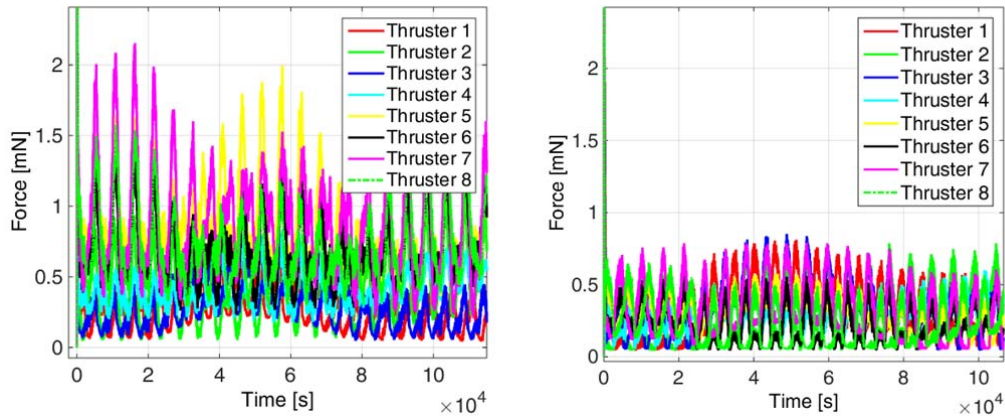


Figure 11 Commanded thrust vector. Left: inline formation. Right: pendulum formation.

Figure 12 shows the 3D residual angular acceleration \mathbf{a} of the leader satellite of the inline formation. The low-frequency spectrum is free of the accelerometer drift since it is rejected by attitude control. Spectral density and time profiles of the pitch acceleration (y axis) show the spectral lines (first and second orbit harmonics) of the FLOF angular acceleration $\dot{\omega}_o$. Spectral lines are chiefly due to orbit eccentricity (first harmonics) and to Earth flatness (second harmonics). In the case of the pendulum formation, spectral lines are dominated by the yaw motion of the satellite-to-satellite line (z axis in Figure 12), and hence of each satellite around the mean formation orbit (see Figure 5). Spectral lines are bounded but, when converting a discrete Fourier transform to spectral density they become unbounded and tend to diverge as soon as the recording length increases. The spectral densities of the y and z axes in Figure 12

show an overshoot around 20 mHz which is absent in the x-axis plot. The overshoot is mainly due to the GNSI noise contribution to the FLOF acceleration $\hat{\mathbf{a}}_o$, which is much more pronounced on the pointing axes. It can be proved that the spectral density S_g of the differential GNSI noise ($\text{m}/\sqrt{\text{Hz}}$) generates angular spectral densities ($\mu\text{rad}/\sqrt{\text{Hz}}$) of this kind

$$\begin{aligned} S_{o_2}(f) &\cong S_{o_3}(f) \cong \sqrt{2} S_g / d_{nom} \cong 7 S_g(f) \\ S_{o_1}(f) &\cong S_{o_2}(f) d_{nom} / r_{nom} \cong 0.03 S_{o_2}(f) \end{aligned} \quad (58)$$

where $d_{nom} = 200 \text{ km}$ is the mean formation distance and $r_{nom} = 6700 \div 6800 \text{ km}$ is the mean orbit radius depending on the formation type (see Table 3). The double derivative of $S_{o_2} \cong S_{o_3}$, plotted in Figure 6, turns out to overlap the optical metrology noise, thus contributing to the poor performance of the pointing control as anticipated in Section 3.4. Improvement of the differential GNSI accuracy seems desirable (see Table 4).

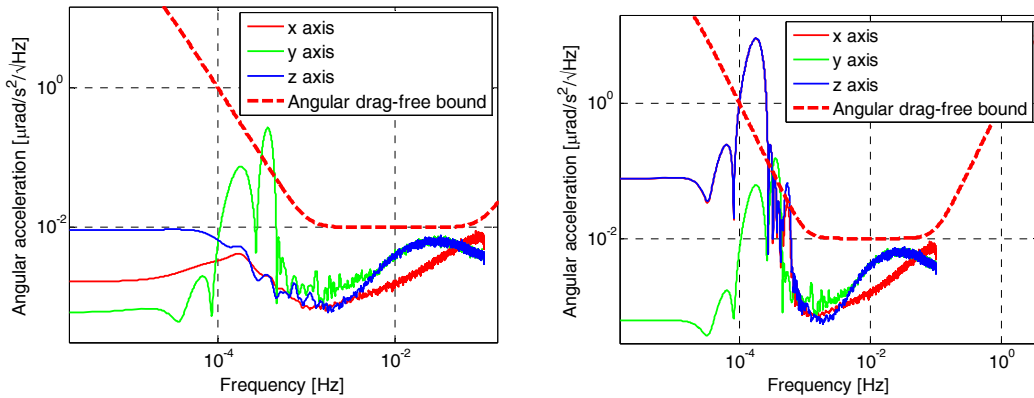


Figure 12 Residual angular acceleration Left: inline formation. Right: pendulum formation.

Similar plots to Figure 12 pertain to the residual angular rates (local angular rate vector $\boldsymbol{\omega}$) as in Figure 13. The spectral density of the pitch rate has been cleaned of the mean orbital value ω_{nom} .

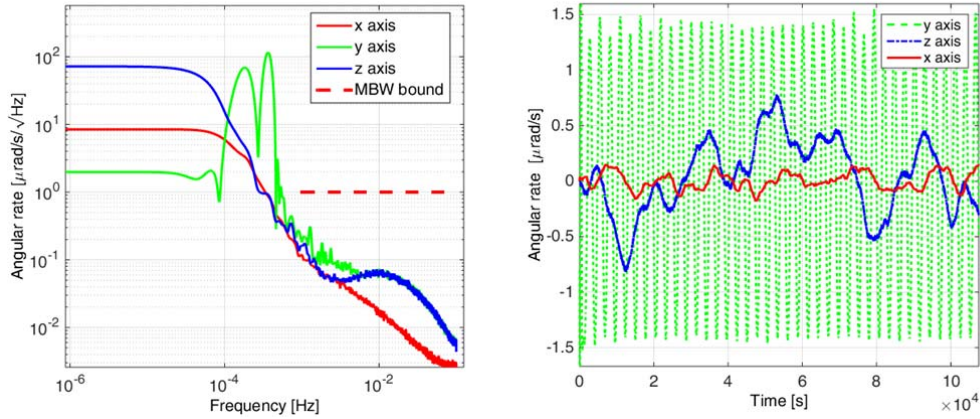


Figure 13 Local angular rate of the inline formation. Left: spectral density. Right: time profile.

Figure 14 shows the spectral density of the residual local attitude (pointing errors and residual roll). In agreement with the lack of design margin in Figure 9, left, pitch and yaw spectral densities do not conform to the MBW bound in Table 1, row 7, equal to $1 \mu\text{rad}/\sqrt{\text{Hz}}$. Actually, as shown in Figure 14, relaxed bounds are made available by science. To be conservative, pointing design has been developed having in mind the worst-case bound $\bar{S}_{q,\min}$ in (2). Mechanism and limits of hybridization become clear by comparing roll and pointing performance in Figure 14. Since roll bound (see Figure 8) is much larger than the pointing one, narrowing the BW of the state predictor below 10 mHz is feasible at the expense of the accelerometer drift rejection (the large overshoot of the roll spectral density). In this way star-tracker noise can be better filtered than optical metrology, and the roll spectral density stays below the bound of Figure 8 with some margin.

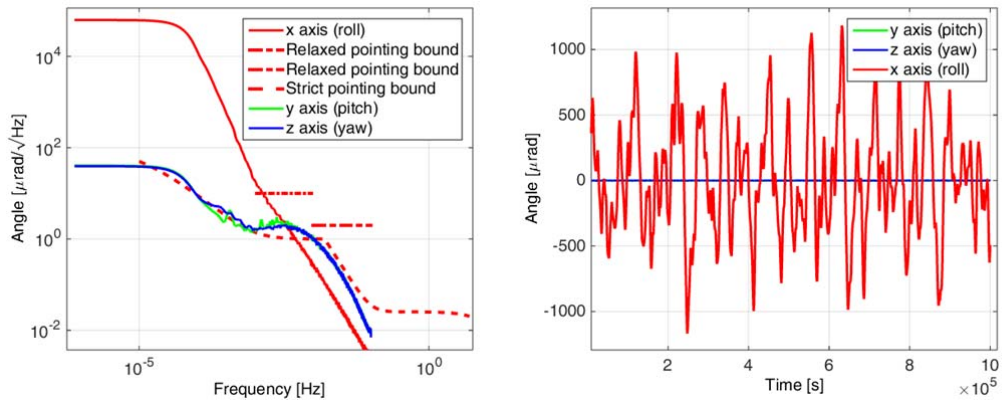


Figure 14 Left: spectral density of the local attitude of the inline formation. Right: Time profile.

As a conclusion, main criticalities and the main recovery modes are summarized in Table 4.

Table 4. Main criticalities and main recovery modes				
No	Criticality	Recovery mode	Figure	Priority
1	Thrust magnitude close to bound for the inline formation.	Thruster layout optimization in parallel to thruster technology finalization/assessment.	Figure 11	Primary issue, but not due to attitude control
2	Residual acceleration low margin above 10 mHz	Improvement of differential GNSI accuracy.	Figure 12	Secondary issue
3	Pointing error spectral density overshoot with respect to worst-case target bound in Table 1	Pointing spectral bound relaxation in parallel to optical metrology finalization/assessment.	Figure 14	Primary issue depending on science metrology

5 Conclusions

The formation attitude control of a scientific mission under study has been outlined, and some critical issues discussed. Formation attitude reduces to independent pointing control of each satellite if optical sensors measuring the satellite misalignment from the satellite-to-satellite line, materialized by a laser beam, are available. Pointing control must be frequency coordinated with drag-free control, since the latter requires that the angular acceleration is ideally zero in a mid-frequency band dictated by scientific measurements. Below this band, acceleration must track the formation frame of reference (FLOF). Drag-free control is designed such to limit the BW of the pointing control and of the FLOF generator from above. This limitation avoids the degradation of the acceleration residuals due the double derivative of the noise of attitude sensors and differential GNSI. In addition, a narrow pointing BW prevents rejection of the low-frequency components of the residual acceleration which are affected by the accelerometer drift. Frequency coordination between angular drag-free and pointing/roll control is implemented by exploiting a hierarchical decomposition of control strategy, embedded models and noise estimators. In practice, drag-free control builds up a fast and

noise-free actuation channel for spacecraft attitude control. To replicate this channel at the level of the embedded model, as required by the Embedded Model Control, the wide-band residual angular acceleration (hybridization signal), which drives the spacecraft attitude, must be carefully estimated and dispatched within the attitude controller. The higher frequency components of this signal substitute optical metrology measurements, which despite being accurate, may degrade the angular acceleration residuals. Simulated results prove and clarify design and criticalities.

6 Appendix

The results presented in the appendix are unpublished.

6.1 Quaternion error equation

Adopting continuous time, the differential equation of the attitude design error $\hat{\mathbf{e}}_q = \hat{\mathbf{q}}^{-1} \otimes \mathbf{q}$ can be written as

$$\begin{aligned} \dot{\hat{\mathbf{e}}}_q(t) &= \frac{1}{2} \hat{\mathbf{e}}_q(t) \otimes \Delta \hat{\boldsymbol{\omega}}(t) \\ \Delta \hat{\boldsymbol{\omega}}(t) &= \boldsymbol{\omega}(t) - \hat{\mathbf{e}}_q^{-1}(t) \otimes \hat{\boldsymbol{\omega}}(t) \otimes \hat{\mathbf{e}}_q(t) \end{aligned} \quad (59)$$

where $\Delta \hat{\boldsymbol{\omega}}$ is the angular rate error with components in the frame defined by \mathbf{q} . $\Delta \hat{\boldsymbol{\omega}}$ can be rewritten with the help of the vectorial part of $\hat{\mathbf{e}}_q$ as

$$\begin{aligned} \Delta \hat{\boldsymbol{\omega}}(t) &= \delta \hat{\boldsymbol{\omega}}(t) + 2 \hat{\mathbf{e}}_q(t) \times \hat{\boldsymbol{\omega}}(t) + o\left(\left|\hat{\mathbf{e}}_q(t)\right|^2\right) \\ \delta \hat{\boldsymbol{\omega}}(t) &= \boldsymbol{\omega}(t) - \hat{\boldsymbol{\omega}}(t) \end{aligned} \quad (60)$$

By replacing (60) in (59), by developing the quaternion product in (59) and by neglecting second order terms in $\delta \hat{\boldsymbol{\omega}}$ and $\hat{\mathbf{e}}_q$, the vectorial differential equation is obtained

$$\begin{aligned} \dot{\hat{\mathbf{e}}}_{q0}(t) &= o\left(\left|\delta \hat{\boldsymbol{\omega}}^T \hat{\mathbf{e}}_q\right|\right), \quad \hat{\mathbf{e}}_{q0}(0) \cong 1 \\ \dot{\hat{\mathbf{e}}}_q(t) &= -\boldsymbol{\omega}(t) \times \hat{\mathbf{e}}_q(t) + \delta \hat{\boldsymbol{\omega}}(t) + o\left(\left|\hat{\mathbf{e}}_q\right|^2, \dots\right), \quad \hat{\mathbf{e}}_q(0) = \hat{\mathbf{e}}_{q0} \end{aligned} \quad (61)$$

The DT version follows from (61) by assuming $|\boldsymbol{\omega}|T \ll 1$.

6.2 Dynamic noise estimator

Consider the embedded model

$$\begin{aligned}\hat{\mathbf{x}}(i+1) &= A\hat{\mathbf{x}}(i) + B\mathbf{u}(i) + G\bar{\mathbf{w}}(i), \quad \hat{\mathbf{x}}(0) = \hat{\mathbf{x}}_0 \\ \hat{\mathbf{y}}_m(i) &= C\hat{\mathbf{x}}(i)\end{aligned}, \quad (62)$$

with $\dim \mathbf{x} = n$, $\dim G = n \times n_w$, $n_w \geq n$, $\dim \mathbf{y} = n_y$. We want to synthesize $\bar{\mathbf{w}}(i)$ through a linear feedback driven by the model error $\bar{\mathbf{e}}_m = \mathbf{y} - \hat{\mathbf{y}}_m$, \mathbf{y} being the measurement vector. Results of [24] and [25] allow establish the following conditions on the existence of static and dynamic stabilizing feedback.

Proposition 3. Static feedback. Given (A, G, C) and a set $\Lambda = \{\lambda_1, \dots, \lambda_n\}$ of symmetric complex eigenvalues, we want find a real L , $n \times n_y$ such that the zeroes of

$$\phi(\lambda) = \det(\lambda I - A + GLC), \quad (63)$$

are exactly the elements of Λ . Only separate necessary and sufficient conditions exist, namely

1) A necessary but not sufficient condition is

$$n_w \times n_y \geq n. \quad (64)$$

2) A sufficient condition is

$$n_w \times n_y > n. \quad (65)$$

Proposition 4. Dynamic feedback. Given (A, G, C) and a set $\Lambda = \{\lambda_1, \dots, \lambda_n, \dots, \lambda_{n+q}\}$ of symmetric complex eigenvalues, we want find an invertible state equation (A_e, L_e, N, L) of order q with real coefficients

$$\begin{aligned}\mathbf{x}_e(i+1) &= A_e \mathbf{x}_e(i) + L_e \bar{\mathbf{e}}_m(i), \quad \mathbf{x}_e(0) = 0 \\ \bar{\mathbf{w}}_e(i) &= N \mathbf{x}_e(i) + L \bar{\mathbf{e}}_m(i)\end{aligned}, \quad (66)$$

such that the zeros of the characteristic polynomial

$$\phi(\lambda) = \det \left(\lambda I - \begin{bmatrix} A - LGC & GN \\ -L_e C & A_e \end{bmatrix} \right) \quad (67)$$

are the elements of Λ . Only separate necessary and sufficient conditions exist, namely:

1) A necessary but not sufficient condition is

$$q(n_w \times n_y - 1) + n_w \times n_y \geq n. \quad (68)$$

2) A sufficient condition is

$$\begin{aligned} q(n_w \times n_y - 1) + n_w \times n_y - \min\{r_y(n_y - 1), r_w(n_w - 1)\} &> n \\ r_y &= q - n_y \text{ floor}(q / n_y), \quad r_w = q - n_w \text{ floor}(q / n_w) \end{aligned} \quad (69)$$

where r_y and r_w are the remainders of q divided times n_y and n_w respectively. \square

Consider the following single-output example with $n = 3$, $n_y = 1$, $n_w = 2$, which corresponds to a generic coordinate of (25), but simplified to include a first-order stochastic dynamics:

$$A = \begin{bmatrix} 1 & 1 & 0 \\ 0 & 1 & 1 \\ 0 & 0 & 1 \end{bmatrix}, \quad G = \begin{bmatrix} 0 & 0 \\ 1 & 0 \\ 0 & 1 \end{bmatrix}, \quad C = [1 \quad 0 \quad 0]. \quad (70)$$

The necessary condition for a static feedback in Proposition 3 is not satisfied since $n_w \times n_y = 2 < n = 3$. Instead, necessary and sufficient conditions of Proposition 4 turn out to be

$$\begin{aligned} 2q + 2 &\geq 3 \\ 2q + 2 - \min\{r_y = 0, r_w\} &= 2q + 2 > 3 \Rightarrow q > 1/2 \end{aligned} \quad (71)$$

and suggest $q \geq 1$, in other terms, the following dynamic feedback

$$\begin{aligned} A_e &= 1 - \delta, \quad L_e = l_e \\ L &= \begin{bmatrix} l_1 \\ l_2 \end{bmatrix}, \quad N = \begin{bmatrix} n_1 \\ n_2 \end{bmatrix}. \end{aligned} \quad (72)$$

The closed-loop state predictor which consists of (70) and (72) is written in compact form as

$$\begin{aligned} \begin{bmatrix} \hat{\mathbf{x}} \\ x_e \end{bmatrix} (i+1) &= \begin{bmatrix} A - GLC & GN \\ -L_e C & A_e \end{bmatrix} \begin{bmatrix} \hat{\mathbf{x}} \\ x_e \end{bmatrix} (i) + \begin{bmatrix} L \\ l_e \end{bmatrix} y(i), \quad \begin{bmatrix} \hat{\mathbf{x}} \\ x_e \end{bmatrix} (0) = \begin{bmatrix} \hat{\mathbf{x}}_0 \\ x_{e0} \end{bmatrix} \\ \hat{y}_m(i) &= [C \quad 0] \begin{bmatrix} \hat{\mathbf{x}} \\ x_e \end{bmatrix} (i) \end{aligned} \quad (73)$$

and the matrices hold

$$\begin{aligned} A_m &= \begin{bmatrix} A - GLC & GN \\ -L_e C & A_e \end{bmatrix} = \left[\begin{array}{ccc|c} 1 & 1 & 0 & 0 \\ -l_1 & 1 & 1 & n_1 \\ -l_2 & 0 & 1 & n_2 \\ \hline -l_e & 0 & 0 & 1 - \delta \end{array} \right], \quad L_m = \begin{bmatrix} 0 \\ l_1 \\ l_2 \\ l_e \end{bmatrix} \\ C_m &= [1 \quad 0 \quad 0 \mid 0] \end{aligned} \quad (74)$$

The six unknown parameters $\Pi = \{\delta, l_1, l_2, n_1, n_2, l_e\}$ are used to fix four closed-loop eigenvalues $\Lambda = \{\lambda_1, \dots, \lambda_4\}$. Let us replace eigenvalues λ_j , $j = 1, \dots, 4$ with their complements $\gamma_j = 1 - \lambda_j$, which implies fixing the polynomial coefficients $c_k \in \mathcal{C} = \{c_0, \dots, c_3\}$ as follows

$$P(\gamma, \mathcal{C}) = \prod_{j=1}^4 (\gamma + \gamma_j) = \gamma^4 + \sum_{j=0}^3 c_j \gamma^j. \quad (75)$$

In the following we assume $0 < \text{Re} \gamma_j \leq 1$. Equality of $P(\gamma, \mathcal{C})$ with the characteristic polynomial $P(\gamma, \Pi)$ of the closed-loop matrix in (74) provides four nonlinear gain equations to be solved

$$\begin{aligned} \delta &= c_3 > 0 \\ l_1 &= c_2 \\ l_e n_1 &= c - l_2 \\ l_e n_2 &= c_0 - l_2 \delta \\ c &= c_1 - l_1 \delta = c_1 - c_2 c_3 = c \end{aligned} \quad (76)$$

Since l_e is a common factor, it is fixed to unit. Thus, the set of the solutions of (76) in Π is a linear variety $\mathcal{V}(l_2, l_e = 1) \subset \Pi$, parameterized by l_2 . The choice of l_2 does not modify the state-predictor input-output properties as the following proposition states.

Proposition 5. The sensitivity $S_m(z) = (y - \hat{y}_m) / y$ and the complementary sensitivity $V_m = 1 - S_m = \hat{y}_m / y$ of the state predictor (73) are invariant in the linear variety $\mathcal{V}(l_2, l_e = 1)$ defined by (76) and by $l_e = 1$.

Proof. The proof follows by observing that $V_m(z)$ and S_m only depend on the coefficients of \mathcal{C} in (75), as follows

$$V_m(z) = \frac{\sum_{k=0}^2 c_k (z-1)^k}{(z-1)^4 + \sum_{j=0}^3 c_j (z-1)^j} \quad \square \quad (77)$$

Therefore the choice of l_2 is just dictated by a simplification aim, and can be restricted to the convex set $\mathcal{K} \subset \mathcal{V}$ defined by

$$\min \{0, c / \delta\} \leq l_2 \leq \max \{c_0 > 0, c / \delta\}, \quad (78)$$

since it includes the following simple solutions

$$\begin{aligned}
l_2 &= 0, \quad n_1 = c, \quad n_2 = c_0 \\
l_2 &= c, \quad n_1 = 0, \quad n_2 = c_0 - c\delta \\
l_2\delta &= c_0, \quad n_1 = c - c_0/\delta, \quad n_2 = 0
\end{aligned} \tag{79}$$

6.3 Comparison with steady-state Kalman filter

It is of interest finding an equivalent Kalman filter of the state predictor (73). As a first step, the gain vector in (72) which has two columns, must be reduced to a single column, but preserving the same sensitivity $S_m = 1 - V_m$ and the same complement V_m as in (77). The following proposition provides the solution.

Proposition 6. There exists a state transformation converting the matrix triple (A_m, L_m, C_m) in (74) to the following triple

$$A_K = \left[\begin{array}{ccc|ccc} 1 & 1 & 0 & 1 & & \\ -l_1 - m_1/\delta & 1 & 1 & 0 & & \\ & -l_2 & 0 & 1 & -\frac{n_2}{n_1}\delta & 0 \\ \hline & n_1/\delta & 0 & 0 & 1 - \delta & \end{array} \right], \quad L_K = \begin{bmatrix} 0 \\ l_1 + n_1/\delta \\ l_2 \\ -n_1/\delta \end{bmatrix}, \quad C_K = C_m. \tag{80}$$

The triple (A_K, L_K, C_K) in (80) takes a structure similar to Kalman filter upon setting $n_2 = 0$, which is admitted by (79).

Proof. The triple (A_K, L_K, C_K) follows from the state transformation

$$\begin{bmatrix} \hat{\mathbf{x}}_K \\ x_{eK} \end{bmatrix} = \left[\begin{array}{ccc|ccc} 1 & 0 & 0 & 0 & & \\ 0 & 1 & 0 & n_1/\delta & & \\ 0 & 0 & 1 & 0 & & \\ \hline 0 & 0 & 0 & -n_1/\delta & & \end{array} \right] \begin{bmatrix} \hat{\mathbf{x}} \\ x_e \end{bmatrix} \tag{81}$$

and by fixing $n_2 = 0$. \square

Actually, the triple (A_K, L_K, C_K) is not a Kalman filter pair since the first entry of L_K is zero, and is replaced by the parameter δ in A_K so as to recover internal stability. This is formally proved below. To this end, we search for appropriate covariance matrices $P > 0$ and $Q \geq 0$, sized $n \times n$, $n = 4$, that, given any gain vector L_K in (80) and any $r^2 > 0$, satisfy the discrete-time Kalman filter equations

$$\begin{aligned}
L_K &= A_K P C_K^T (C_K P C_K^T + r^2)^{-1} \\
P &= (A_K - L_K C_K) P (A_K - L_K C_K)^T + Q + L_K r^2 L_K^T
\end{aligned} \tag{82}$$

As matter of fact, given the matrix triple (80), no P and Q exist satisfying (82), meaning that the state predictor (73) belongs to a class of dynamic systems which cannot be reduced to a Kalman filter.

Theorem 3. Given any triple (A_K, L_K, C_K) in (80), equation (82) does not admit any solution for P and Q .

Proof. Using the Kronecker product \otimes , equation (82) can be rewritten as a linear equation

$$\mathbf{y}_K = r^2 \begin{bmatrix} L_K \\ 0_{n^2} \end{bmatrix} = \begin{bmatrix} (C_K \otimes (A_K - L_K C_K)) D & 0 \\ -(I_{n^2} - (A_K \otimes (A_K - L_K C_K))) D & D \end{bmatrix} \begin{bmatrix} \text{vech}(P) \\ \text{vech}(Q) \end{bmatrix} = F_K \mathbf{p}, \tag{83}$$

where $\text{vech}(P)$ and $\text{vech}(Q)$ are the $m = n(n+1)/2$ vectors of the upper diagonal part of the symmetric matrices P and Q , D is a suitable $n^2 \times m$ matrix (called duplication matrix) such that $\text{vec}(P) = D \text{vech}(P)$, where $\text{vec}(P)$ is the n^2 -sized vector of the columns of P , 0_{n^2} is zero vector of size n^2 and I_{n^2} is an identity matrix of size n^2 . The LHS vector \mathbf{y}_K in (83) is sized $n(n+1)$ like the unknown vector \mathbf{p} in the RHS. Thus, the equation matrix F_K is square as expected. Using symbolic algebra, one can prove that \mathbf{y}_K does not belong to the range of F_K , i.e.

$$\mathbf{y}_K \notin \mathcal{R}(F_K), \tag{84}$$

and the Theorem is proved. \square

The result (84) appears to be rather strong, as it does not involve the positive (semi-)definiteness of P and Q . The result holds also for non-definite matrices.

To conclude, Kalman filter exists for the triple (A, G, C) , but it adds a parasitic noise component to the first equation in (74), which is contrary to the first line of G as it is equal to zero. The parasitic noise is such to reduce the relative degree of the complementary sensitivity V_m to one (instead of two for the dynamic feedback), which is detrimental to noise and neglected dynamics rejection.

7 Acknowledgments

Part of the work of the authors from Politecnico di Torino has been done under a sub-contract with the European Space Agency (ESA), Thales Alenia Space Italia, Turin, Italy, being the prime contractor. The second author is a Ph.D. student at Politecnico di Torino funded under the ESA Networking/partnering Initiative (NPI). Remarks and suggestions of anonymous reviewers are greatly acknowledged.

8 References

- [1] M. Fehringer, G. André, D. Lamarre and D. Maeusli, “GOCE and its gravity measurement system”, *ESA Bulletin*, Vol. 133, February 2008, p. 15-23.
- [2] B.D. Tapley, S. Bettadpur, M. Watkins and C. Reigber, “The gravity recovery and climate experiment: Mission overview and early results”, *Geophys. Res. Lett.*, Vol. 31, No. 9, May 2004.
- [3] E. Canuto, A. Molano and L. Massotti, “Drag-free control of the GOCE satellite: noise and observer design”, *IEEE Trans. Control Systems Technology*, Vol. 18, No.2, March 2010, pp. 501-509.
- [4] E. Canuto “Drag-free and attitude control for the GOCE satellite”, *Automatica*, Vol. 44, No. 7, 2008, pp. 1766-1780.
- [5] G. Sechi, M. Buonocore, F. Cometto, M. Saponara, A. Tramutola, B. Vinai, G. Andrè and M. Fehringer “In-flight results from the drag-free and attitude control of GOCE satellite”, *Preprints 18th IFAC World Congress*, Milan (Italy), 28 August-2 September 2011, pp. 733-740.
- [6] J. Herman, D. Presti, A. Codazzi, and C. Belle “Attitude control for GRACE the first low-flying satellite formation”, *Proc. of the 18th Intern. Symposium on Space Flight Dynamics* (ESA SP-548).
- [7] S. Cesare, S. Mottini, F. Musso, M. Parisch, G. Sechi, E. Canuto, M. Aguirre, B. Leone, L. Massotti and P. Silvestrin, “Satellite formation for a next generation gravimetry mission”, in R. Sandau et al. eds., *Small satellite missions for Earth observations*, Springer, Heidelberg, pp. 125-134, 2010.
- [8] B. Polle et al. “Robust INS/GPS hybrid navigator demonstrator design for launch, re-entry and orbital vehicles” *Proc. 7th Int. ESA Conf. on Guidance, Navigation and Control*, 2-5 June 2008, Tralee, Ireland.
- [9] E. Canuto, L. Colangelo, M. Buonocore, L. Massotti and B. Girouart “Orbit and Formation control for low-Earth-orbit gravimetry drag-free satellites”, *Proc. of the Inst. of Mechanical Engineers, Part G: J. of Aerospace Engineering*, on-line published, September 21, 2014, doi:10.1177/0954410014548236.
- [10] Canuto “Embedded Model Control: outline of the theory”, *ISA Transactions*, Vol. 46, No. 3, 2007, pp. 363-377.
- [11] E. Canuto, W. Acuna-Bravo, A. Molano and C. Perez “Embedded Model Control calls for disturbance modeling and rejection”, *ISA Transactions*, Vol. 51, No. 5, 2012, pp. 584-595.
- [12] E. Canuto, W. Acuna-Bravo and C. Perez “Robust control stability using the error loop”, *Int. J. of Mechatronics and Automation*, Vol. 3, No. 2, 2013, pp. 94-109.

- [13] E. Davison “The output control of linear time invariant multivariable systems with unmeasurable arbitrary disturbances”, *IEEE Trans. Automatic Control*, Vol. 17, No. 5, 1972, pp. 621-630.
- [14] B.A. Francis “The internal model principle of control theory”, *Automatica*, Vol. 12, No. 5, 1976, pp. 457-465.
- [15] H. Wong, H. Pan and V. Kapila “Output feedback control for spacecraft formation flying with coupled translation and attitude control”, *Proc. 2005 American Control Conf.*, Portland, Oregon, June 8-10, 2005, pp. 2419-2426.
- [16] H. Cho and F. E. Udwadia “Explicit control force and torque determination for satellite formation-keeping with attitude requirements”, *J. of Guidance, Control and Dynamics*, AIAA early ed., DOI: 10.2514/1.55873.
- [17] T. Lee “Relative attitude control of two spacecrafts on SO(3) using Line-of-Sight observations”, *Proc. 2012 American Control Conf.*, Montreal, Canada, June 27-29, 2012, pp. 167-172.
- [18] M.C. VanDyke and C. D. Hall “Decentralized coordinated attitude within a formation of spacecraft”, *J. of Guidance, Control and Dynamics*, Vol. 29, No. 5, 2006, pp. 1101-1109.
- [19] L.B. Freidovich and H.K.Khalil “Robust feedback linearization using extended high-gain observer”, *Proc. 49th IEEE Conf. on Decision and Control*, San Diego, CA, December 13-15, 2006, pp. 983-988.
- [20] S. Di Gennaro “Tracking control using attitude measurements for flexible spacecrafts in presence of disturbances”, *Proc. 43rd Conf. on Decision and Control*, Bahamas, December 14-17, 2004, pp. 2123-2128.
- [21] Y.Xia, Z. Zhu, M. Fu and S. Wang “Attitude tracking of rigid spacecraft with bounded disturbances”, *IEEE Trans. on Industrial Electronics*, Vol. 58, No. 2, 2011, pp. 647-659.
- [22] E. Canuto and L. Colangelo “Angular drag-free control and fine satellite-to-satellite pointing for the Next Generation Gravity Missions“, in *Proc. of the 13th European Control Conference*, Strasbourg, France, 2014, June 24-27, 2014, pp. 3017-3022.
- [23] E. Canuto, A. Molano Jimenez and C. Perez Montenegro “Disturbance rejection in space applications: problems and solutions“, *Acta Astronautica*, vol. 72, 2012, pp. 121-131.
- [24] A. Eremenko and A. Gabrielov “Pole placement by static output feedback for generic linear systems”, *SIAM J. Control and Optimization*, Vol. 41, No. 1, 2002, pp. 3013-312.
- [25] J. Rosenthal and J. C. Willems “Open problems in the area of pole placement”, in *Open Problems in Mathematical Systems and Control Theory, Communication and Control Engineering Series*, 1998, pp. 181-191, Springer-Verlag.
- [26] C. Mohtadi “Bode’s integral theorem for discrete-time systems”, *IEE Proceedings, Part D*, Vol. 137, No. 1999, pp. 57-66.
- [27] J. S. Freudenberg and D. P. Looze “Right half-plane poles and zeros and design tradeoffs in feedback systems”, *IEEE Trans. Automatic Control*, Vol. 30, No. 6, June 1985, pp. 555-565.
- [28] H. K. Khalil, *Nonlinear systems*, 2nd ed., Prentice–Hall, Upper Saddle River, NJ, 1996.
- [29] H. K. Khalil, “High-gain observers in nonlinear feedback control”, *Proc. 2008 Int. Conf. on Control, Automation and Systems*, Seoul, Korea, 2008.